November 21, 2020

Dear Rebecca Hodge,

On the behalf of co-authors, I would like to thank you for the thorough and constructive comments. They were very useful to improve the overall quality and readability of the manuscript. We have tried answering all the suggestion and comments made by you and revised the manuscript accordingly.

We have enclosed the following with this letter ;

— a detailed response

— a difference file showing the changes in the previous version of the manuscript in response to the comments

I hope this revised manuscript will be considered suitable for publication in Esurf.

Your truly

Kumar Gaurav

Answer to Dr. Rebecca Hodge

Text in black is the comments

Text in blue is the author's response

Line no: 30 It's possible to use these equations to explain two slightly different things. One is how channel properties at mean flow change between different locations along a river. The other is how, at a specific location, the properties of the channel change as discharge changes. Which are you referring to? Section 3 implies that is the former, in which case you need to specify which discharge you are referring to (mean/bankfull/flood).

Yes, in our case we are using the width-discharge regime equation to explain the channel properties at formative discharge between different locations along a river reach. The discharge that we are referring corresponds to bankfull discharge. Accordingly we have specified this in the revised manuscript.

Line no: 67 I'm not sure what you mean by 'unique' - specific to these particular rivers?

We have removed 'unique' from the sentence.

Line no: 69 By river width, do you mean the width of the water, or the width between the banks (water plus exposed sediment, typically identified as the edge of the floodplain vegetation)? This might be obvious to you, but I can imagine that different readers might assume

Our river width corresponds to the width of the water in a thread. In braided river, this is usually taken from margin to margin of an individual thread. As already explained in the manuscript, we consider braided threads as a collection of individual threads and we treat them separately to extract the wetted width observed from satellite images.

Line: 85 In Fig 1, I wouldn't say that the discharge looks constant in the unshaded region. Consider rewording.

Thank you for highlighting this. We have modified the sentence in the revised manuscript.

Line no: 89 Returning to my previous point, was Lacey comparing width at mean discharge between different locations, or variations in width with discharge at a specific location?

A quick answer to this question is regime channels. The measurements reported in Lacey 1930 and used by him to derive Lacey's law firstly come from studies performed on different Indian irrigation canals by Kennedy and Lindsey at the turn of the 20th century. The measurements reported are values measured for different "experiments" where controlled constant discharges where flowing through an irrigation channel and the corresponding hydraulic geometry mea-

sured. Lacey also compares these measurements to a small set of measurements performed on Egyptian canals. Then he shows that his law also works for regime data gathered from different rivers of India (the Ganga, Irrawady, Chenab etc). There is a very interesting discussion on the way engineers empirically tried to "fit" the Chenab river into a single stable channel that falls on the $W \propto Q^{0.5}$ line.

Line no: 104 Explain the implication in terms of later estimates of discharge - I think that using 0.3 means that your estimates are the lowest possible discharge for a given width?

It appears there are some misunderstandings here. Equation 4 predicts the width of a threshold channel to imposed discharge. According to this equation, width of a threshold channel scales as a square root of discharge. Parameters in the pre-factor depend on fluid and sediment properties. Some of these parameters such as water and sediment density, friction angle are approximately constant. However, in rivers, the other parameters such as the median grain size, turbulent friction coefficient and Shield parameter (θ_t) vary significantly. It has been found that the Shield parameter ranges between 0.03-0.3, depending on the Reynolds number on grain scale (Métivier et al., 2017). As we have already mentioned in the manuscript that Delorme et al. (2017), obtained an experimental value of Shield parameter 0.25 for silica grains of size 150 micron. As the typical grain-size of the Himalayan rivers vary between 100-300 micron, we have taken the upper value of $\theta_t = 0.3$ as a conservative estimate. Since this value is experimentally obtained for the grain size that is comparable to the sediment size of the Himalayan Foreland river, it provides more confidence. However for a similar discharge, using a lower value of θ_t (i.e; 0.1 or lesser) would lead to a slightly wider cross-section of a channel. Further, it is observed that, at a given discharge, width of a natural channel scales in a similar fashion to that of threshold channel. However, natural rivers are much wider (about a factor of 2 in our case) than the threshold channel. Though using a lowest possible value of θ_t would not result to a closer match to the width of a natural channel. Therefore in this study, we have adjusted the pre-factor to best-fit the data points while keeping the theoretical exponent to establish a semi-empirical width-discharge curve. Later we use this curve to estimate discharge from the measurement of channel's width on remote sensing images.

Line no: 115 From this I assumed that you would be using the curve in Fig 2 in this paper, but I see later that this is not the case. This needs to be more clearly explained. (See also comment on page 12)

We are using the same curve shown in Fig 2 to estimate discharge from thread's width extracted from satellite images. This we have also explained in lines 117-121. We have clearly written that the threshold theory well predicts the exponent of the width-discharge relationship of the

Himalayan rivers but not the pre-factor. Threads of the Himalayan rivers are wider (about factor of 2) than the theoretical prediction. To go further we have adjusted the pre-factor to the data while keeping the theoretical exponent to establish a generalised semi-empirical regime curve for the Himalayan rivers. Finally, we use this "semi-regime curve" to estimate discharge from satellite images.

Line no: 116 Further details are needed. Explain which width (wetted or total channel width), and which discharge (mean/bankfull/flood).

Done. We have measured the wetted width of the threads using an Acoustic Doppler Current Profiler (ADCP) in the field. Most of our measurements were acquired during the period when rivers of the Himalayan Foreland usually flow at their bankfull discharge.

Line no: 127 include the pixel size of the different datasets

Done, we have included this in subsection 4.2 (width extraction). The spatial resolution of the IR band of Landsat image is 30 meters. For Sentinel-1 images we get a spatial resolution of 60 meters after the removal of speckle noise. We then resampled this to (30×30)m square pixel.

Figure 2 caption: As with the text, you need to explain which width and discharge you are referring to.

Done

Line no: 184 Is this a manual or automated procedure? Is this one that you have developed, or adopted from elsewhere? You need to include more information about this in the main text.

This is an automated procedure that we have developed to measure the wetted width of individual threads from remote sensing images. This is already mentioned in section 4.2 (lines 144-146). We have also provided the detailed description of the algorithms that we have developed to split the water and non-water pixels from the satellite images (section 4.2) and eventually to measure channel width in Appendix B (Satellite image processing).

Line no: 210 Define what you mean by relative error.

Relative error is a measure of precision. We have calculated this by taking the ratio of the absolute error between manually and automatically measured width to automatically measured width of a thread. As suggested, we have added a line to define the relative error.

Line no: 219 It's not clear to me that the geometric mean is necessarily the most probable value. I would have said that the mode is the most probable value, as that is the value that the largest number of widths have.

We agree and restrict to write "most probable" width, instead we use geometric mean as a

"representative width". We have used geometric mean because it is less affected by extreme values in a skewed distribution.

Line no: 231 I thought from earlier that you were going to use the equation in Fig 2, but I see now that you can't use that because it contains grain size. This needs to be explained either earlier, or here. Somewhere you also need to explain how Gaurav et al established their regime relation

In the revised manuscript we have explained (line no: 117-123) how Gaurav et al has established the width-discharge regime curve for the Himalayan Foreland rivers. Yes, we have used equation 4 as explained in Fig 2. We have rearranged the equation 4 to estimate discharge from the measurement of width. To explain this let me rewrite how equation 6 was obtained from equation 4;

$$\frac{W}{d_s} = \left[\frac{\pi}{\mu}\left(\frac{\theta_t(\rho_s - \rho_f)}{\rho_f}\right)^{0.25}\sqrt{\frac{3C_f}{2^{3/2}\mathcal{K}\,[1/2]}}\right] Q_*^{0.5} \tag{1}$$

where $Q_* = Q_w/(d_s^2\sqrt{gd_s})$ is the dimensionless water discharge. Please refer to the manuscript for the description of other parameters. The Himalayan River scales according to threshold theory (1), but not the pre-factor (in square bracket). Now we keep the exponent as predicted by theory and adjust the pre-factor to best-fit our data points. The resulting width-discharge curve reads;

$$\frac{W}{d_s} = \alpha\, Q_*^{0.5} \tag{2}$$

where α is the best-fit coefficient obtained from adjusting the pre-factor. This semi-empirical curve (Eqn. 2) has the theoretical exponent and empirical pre-factor.

Now we rearrange equation 2 to get Q;

$$W/d_s = \alpha\,(Q_w/d_s^2\sqrt{gd_s})^{0.5} \tag{3}$$

Finally we get;

$$Q_w = \left(\frac{W_m}{\alpha}\right)^2\sqrt{(gd_s)}, \tag{4}$$

Line 232 It's not clear to me from this how you get a value for alpha if you only have the width measurements.

Already explained above. Also in the revised manuscript (line 240) we have defined 'α'. "This is the best-fit coefficient, an empirical value obtained from fitting the prefactor of the regime curve (Eq.4)"

Figure 9 Need to explain how error bars are calculated.

Explained in the caption.

Table 1 Need to explain how errors are calculated.

Explained in the caption.

Line no: 248 But in some cases there is a clear annual cycle, so the image does seem to better represent the monthly discharge. It would be useful to explore why the predicted discharge varies annually at some sites, and is constant at others. I assume that it is related to the shape of the channel, and hence how much the wetted width varies with discharge?

Thank you for highlighting this. We have written this in revised manuscript (line: 249-252). Though figure 9 shows annual cycle for Indus, Cheenab, and Teesta River, but it is not observed in the remaining rivers. As already explained in the discussion, these rivers are highly regulated (lines 296-300), and also discharge records for the Teesta at Kaunia (1969 - 1975) and at Anderson bridge (1965 - 1971) are available only for 6 and 7 years respectively (Table A2 in appendix). Similarly, the records for both Chenab and Indus rivers extend over 7 years only (1973 - 1979). These measurements are old and thus we refrain from commenting on the observed annual cycle. Further, we can also observe a strong declining trend of monthly discharges of the Indus, Chenab and Teesta rivers (figures C2 and C3 in appendix, in the manuscript). This validates that the hydrology of these rivers may have evolved since these records were established.

Line no: 270 This still doesn't quite explain to me why the wetted width doesn't vary with discharge in some channels. Doesn't it depend on the channel shape?

To answer this lets explain the cross-section geometry of a braided thread. Figure 1 illustrate the cross-section of a braided thread measured in the field using Acoustic Doppler Current Profiler (ADCP). This high resolution bathymetric profile enables us to identify the two different threads (see the velocity cells) separated by a region of very shallow flow depth (submerged bar). As a consequence, discharge is not carried through the width that is observed from the top, but only through the region where we observe the velocity cells. It is important to notice here that the geometry of this thread must have been set at the formative discharge. During low flow usually threads maintain their flows without modifying the existing geometry.

Currently satellite images allow us to measure the top width of water surface, this is perhaps one of the reasons why our estimated of average monthly discharge is mostly overestimated then the in-situ value and does not show much variability.

Line no: 278 I'm confused by this section. You seem to be arguing that the measured width, and

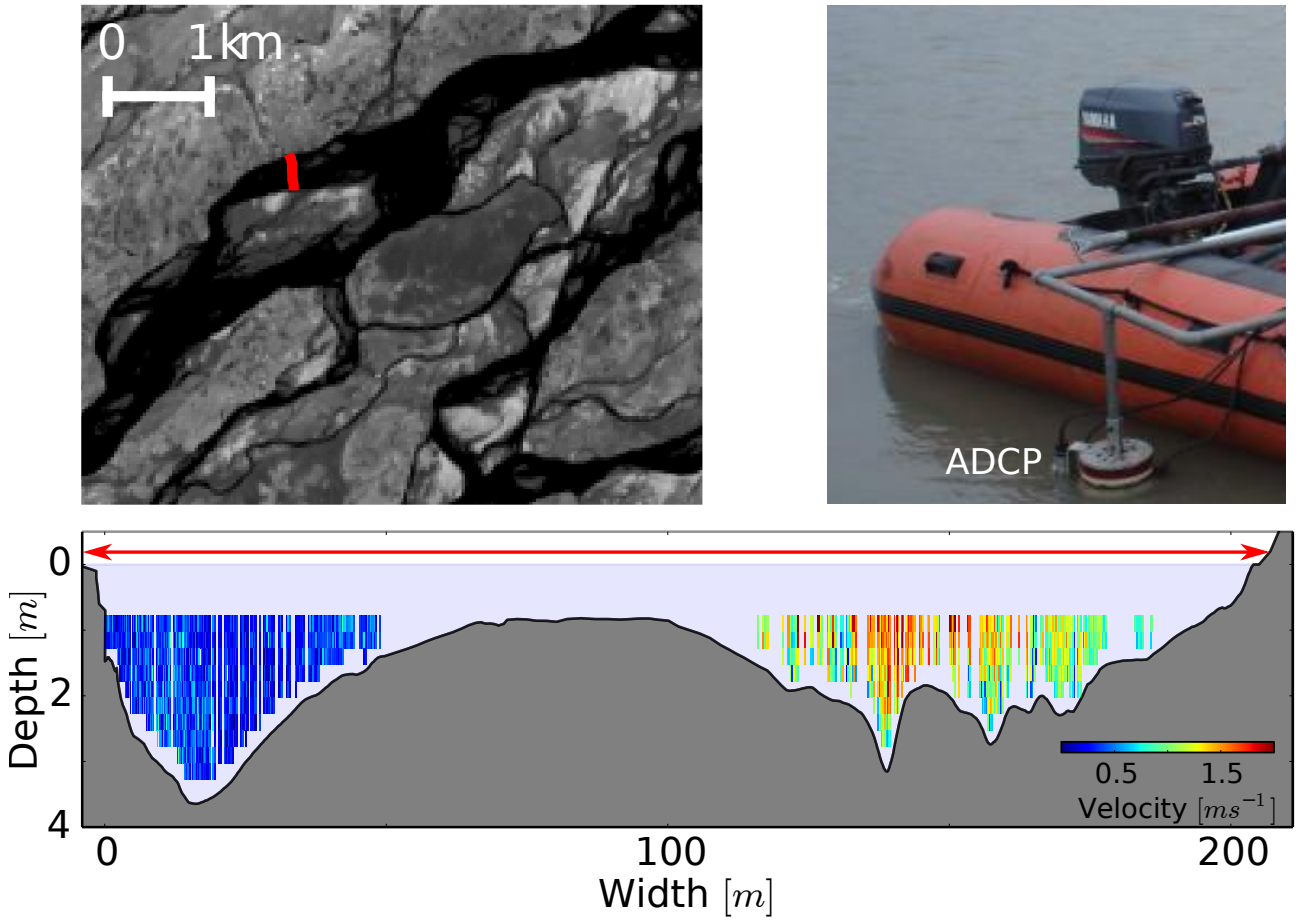

Figure 1: Velocity profile measured using and ADCP across a braided thread of the Kosi River in the Himalayan Foreland. Red horizontal line with arrow is to illustrate the top water surface. Colors with different intensities show the magnitude of velocity (m/s)

hence discharge, doesn't vary between months. I don't agree with this, because the predicted discharge clearly does vary between months at some sites in Fig 9. Furthermore, Fig C2 and C3 seem to show that your data do reproduce observed differences between months. I'm not sure what Fig C1 is meant to show.

Justification to both the points are explained above. To comment on the observed variability in some stations (Indus, Cheenab, and Teesta) we modified the discussion section in the revised manuscript.

Line no: 283 Again, I don't agree with this interpretation of Fig 9

Now we have modified this sentence and write, except for the rivers (Indus, Chenab and Teesta) we have old and limited records of in-situ discharge. "We observe that the estimated discharges from images are nearly constant during the monsoon period, with only small fluctuations around their mean" We think this justifies our interpretation of fig 9.

line no: 291 Are the images and the discharge data from the same time period? The datasets referred to in the methods covered a wide range of time periods. Please clarify here.

The in-situ discharge data and images are not from the same time period. This is already mentioned in the manuscript in sub-section 4.1 and Table A2 in the Appendix.

Line no: 317 Provide a bit more information in the main text about how the different estimates compare

Done

Line no: 323 Any river, or just those above a certain width?

Since our width-discharge regime curve is established from numerous channels of different sizes, we believe it can be used to approximate the formative discharge of any rivers of the Himalayan Foreland.

Line no: 325 Which measurements? The new data in this paper are from all months. You need to make it clear that this paragraph is all referring to previous work.

We have explained the measurements and accordingly modified the sentences to make it more clear.

Line no: 328 formative or instantaneous?

Formative

Line no: 339 You took width measurements from a range of different data sources (images/ASAR), but have not compared them. Are some data sources more reliable than others?

This is one of the limitations, we could not compare our threads width extracted from Landsat and SAR images. Since the temporal resolution of both the images are different we could not find common acquisition dates for both the datasets. Further it doesn't make much sense to compare the measurements obtained from images of two different dates. As already discussed in the manuscript (129-135), that SAR sensors can acquire uninterrupted image of the Earth's surface even during the bad weather conditions. This is an important dataset that allows us to monitor rivers during the monsoon period, where optical images are affected by cloud cover and strong rainfall.

Appendix For each location in C2 and C3, use the same vertical scale

Done

References

Delorme, P., Voller, V., Paola, C., Devauchelle, O., Lajeunesse, É., Barrier, L., and Métivier, F. (2017). Self-similar growth of a bimodal laboratory fan. *Earth Surface Dynamics*, 5:239–252.

Métivier, F., Lajeunesse, E., and Devauchelle, O. (2017). Laboratory rivers: Lacey's law, threshold theory, and channel stability.

Coupling threshold theory and satellite image derived channel width to estimate the formative discharge of Himalayan Foreland rivers.

Kumar Gaurav[1], François Métivier[2], AV Sreejith[3], Rajiv Sinha[4], Amit Kumar[1], and Sampat Kumar Tandon[1]

[1]Indian Institute of Science Education and Research, Bhopal,462066, M.P, India
[2]Institute de Physique du Globe de Paris, 1 Rue Jussieu, 75005 Paris cedex 05, France
[3]School of Mathematics and Computer Science, Indian Institute of Technology, Goa, 403401, Goa, India
[4]Department of Earth Sciences, Indian Institute of Technology, Kanpur, 208016 UP, India

Correspondence: K.Gaurav (kgaurav@iiserb.ac.in)

Abstract. We propose an innovative methodology to estimate the formative discharge of alluvial rivers from remote sensing images. This procedure involves automatic extraction of the width of a channel from Landsat Thematic Mapper, Landsat 8, and Sentinel-1 satellite images. We translate the channel width extracted from satellite images to discharge by using a width-discharge regime curve established previously by us for the Himalayan Rivers. This regime curve is based on the threshold theory, a simple physical force balance that explains the first-order geometry of alluvial channels. Using this procedure, we estimate the discharge of six major rivers of the Himalayan Foreland: the Brahmaputra, Chenab, Ganga, Indus, Kosi, and Teesta rivers. Except highly regulated rivers (Indus and Chenab), our estimates of the discharge from satellite images can be compared with the mean annual discharge obtained from historical records of gauging stations. We have shown that this procedure applies both to braided and single-thread rivers over a large territory. Further our methodology to estimate discharge from remote sensing images does not rely on continuous ground calibration.

Keywords: Himalayan Foreland; regime curve; threshold theory; formative discharge

1 Introduction

The measurement of river discharge is necessary to investigate channel morphology, sediment transport, flood risks, and to assess water resources. Despite this, the discharge of many rivers remains unknown, especially those located in sparsely populated regions, at high latitudes, or in developing countries. Even now, the discharge is measured at sparsely located stations along a river's course (Smith and Pavelsky, 2008; Andreadis et al., 2007). Between measurement stations, the discharge is interpolated using routine techniques (Smith and Pavelsky, 2008). Further, these local measurement stations are installed where the river flows as a single-thread channel and has a stable boundary. This is often not the case for braided rivers, where the flow

is distributed through multiple and mobile threads (Smith et al., 1996; Ashmore and Sauks, 2006). Braided rivers are therefore often not gauged; and where these exist, the gauging stations are located at places like dams with artificially regulated flow. This hinders our ability to assess discharge in the individual threads of a braided river.

To overcome this problem, and to minimise the costs related to discharge measurement, methodologies have been developed to use remote sensed images to estimate the instantaneous discharge of rivers (Smith et al., 1996; Smith, 1997; Alsdorf et al., 2000; Ashmore and Sauks, 2006; Alsdorf et al., 2007; Marcus and Fonstad, 2008; Papa et al., 2010, 2012; Gleason and Smith, 2014; Durand et al., 2016; Gleason et al., 2018; Allen and Pavelsky, 2018; Moramarco et al., 2019; Kebede et al., 2020). These studies establish rating relationships between some image-derived parameters (width, water level or stage, slope), to the instantaneous discharge measured in the field (Leopold and Maddock, 1953). Equations that define the hydraulic geometry of a channel relate width (W), average depth (H), and slope (S) of a channel to ~~its~~ the bankfull discharge (Q) according to:

$$W = aQ^{e}, \tag{1}$$

$$H = bQ^{f}, \tag{2}$$

$$S = cQ^{-g}, \tag{3}$$

where a, b, c, e, f, g are site specific constants and exponents. The available methods, based on remote sensing data, to estimate the discharge of a river therefore cannot be extrapolated to other rivers, or even to other locations on the same river. Moreover, as these rating curves vary significantly between locations, they must be established for each location independently. For example, Smith et al. (1995); Smith (1997); Smith and Pavelsky (2008) and Ashmore and Sauks (2006), used synthetic aperture radar and ortho-rectified aerial images to estimate discharge in braided rivers. They related the image derived effective width of a braided river to the discharge at a nearby gauge station to establish a relationship of the form of equations 1, 2, & 3. Their approach provides an estimate of the total discharge in a braided river, at a given section. However, this technique is site specific and assumes that the river bed does not change over time.

Few attempts have been made to overcome these limitations; for example Bjerklie et al. (2005) used aerial orthophotographs and SAR images to estimate discharge in various single-thread and braided rivers. To estimate the discharge they extracted the maximum water width at a given river reach. They then combined the image-derived channel widths with channel slopes obtained from topographic maps, and a statistical hydrologic model. They reported standard errors of $50-100\,\%$. However, after using a calibration function based on field observation, the error reduced to values as low as $10\,\%$. Later, Sun et al. (2010) used Japan Earth Resource Satellite-1 (JERS-1) SAR images to measure the effective width of the Mekong River at the Pakse gauging station in Laos. They used rainfall-runoff model to estimate the discharge from the image-derived width and suggested that using this procedure, the discharge could be estimated in any ungauged river basin within an acceptable level of accuracy. They established a close agreement between the measured discharge of the Mekong River at Paske station and the model estimate to the $90\,\%$ uncertainty level. As discussed earlier by Bjerklie et al. (2005), later Sun et al. (2010) indicated that the precision can be improved by calibrating the rainfall-runoff model with a hydraulic geometry relation, and that a calibrated rainfall-runoff model can be used to estimate the discharge in any ungauged river using the measured width only. Gleason and

Smith (2014) have suggested that the discharge of a single-thread river can be estimated from satellite images only, without any ground measurement. They plotted the exponents and coefficients of hydraulic regime equations established at 88 different gauging stations along six rivers in the United States, and found that the exponents and coefficients are correlated. Recently Kebede et al. (2020) have used Landsat images to estimate daily discharge of the Lhasa River in the Tibetan Plateau. They have used image derived hydraulic variables to compute the discharge by using modified Manning equation and rating curves established from the in-situ measurement of width and discharge.

The studies discussed above attempt to address the issue of site-specificity, and propose methods to estimate discharge without empirical calibration. However Bjerklie et al. (2005), and Sun et al. (2010) also show that a better accuracy in discharge prediction can only be achieved with some calibration to ground measurements. Therefore, a physically robust method to resolve the site-specificity of rating curves remains to be described.

To address this issue of site-specificity, we have developed a semi-empirical width-discharge regime relation based on the threshold theory and field measurement of various braided and meandering rivers on the Ganga and Brahmaputra plain (Seizilles et al., 2013; Métivier et al., 2016; Gaurav et al., 2017). According to this relation, threads of braided and meandering rivers share a common width-discharge regime relationship. We therefore hypothesise that, this ~~"unique"~~ regime equation can be used to estimate the first order discharge of any river (braided or meandering) flowing on the Ganga and Brahmaputra plains, and perhaps on the entire Himalayan Foreland, if wetted width of the river channels is known. This study can also be used for various applications such as: (i) to monitor the downstream evolution of discharge, (ii) to fill the data gap in between the gauge stations separated over a long distance, (iii) to construct the time-series and trend analysis of discharge variation, and (iv) to identify the critical reaches in rivers that are under stress due to excessive extraction of water for agriculture, industrial or domestic supply.

2 Hydrology of the Himalayan Rivers

Many rivers flowing on the Indus-Ganga-Brahmaputra alluvial plains are perennial and have their source in the Himalaya and Tibetan Plateau. Flow of these rivers is primarily determined by snowmelt and rainfall during the Indian summer monsoon (Singh and Jain, 2002; Thayyen and Gergan, 2010; Bookhagen and Burbank, 2010; Andermann et al., 2012; Khan et al., 2017). However, the contribution of rainfall and snowmelt in the discharge of the Himalayan rivers vary significantly along the orogenic strike. For example, on an annual timescale, snowmelt contributes about 15-60% of discharge in the western Himalayan rivers, whereas it is less than 20% in the eastern Himalayan rivers (Bookhagen and Burbank, 2010). These rivers experience a strong seasonal variability in their discharge, for instance rainfall during the Indian summer monsoon (June-September) constitutes about 60-85% of the eastern and about 50% of the annual discharge of the western Himalayan catchments.

A closer look into the hydrographs of the Himalayan rivers reveals two distinct flow regimes (Fig. 1). A clear separation of discharge during the summer monsoon and rest of the period can be observed. From May to October, most of the Himalayan rivers flow at their peak discharge due to intense and prolonged rainfall and glacier melting in the catchment; whereas, in lean

period (November-April), they carry relatively less dischargewhich remains almost constant with small fluctuations around the mean value.

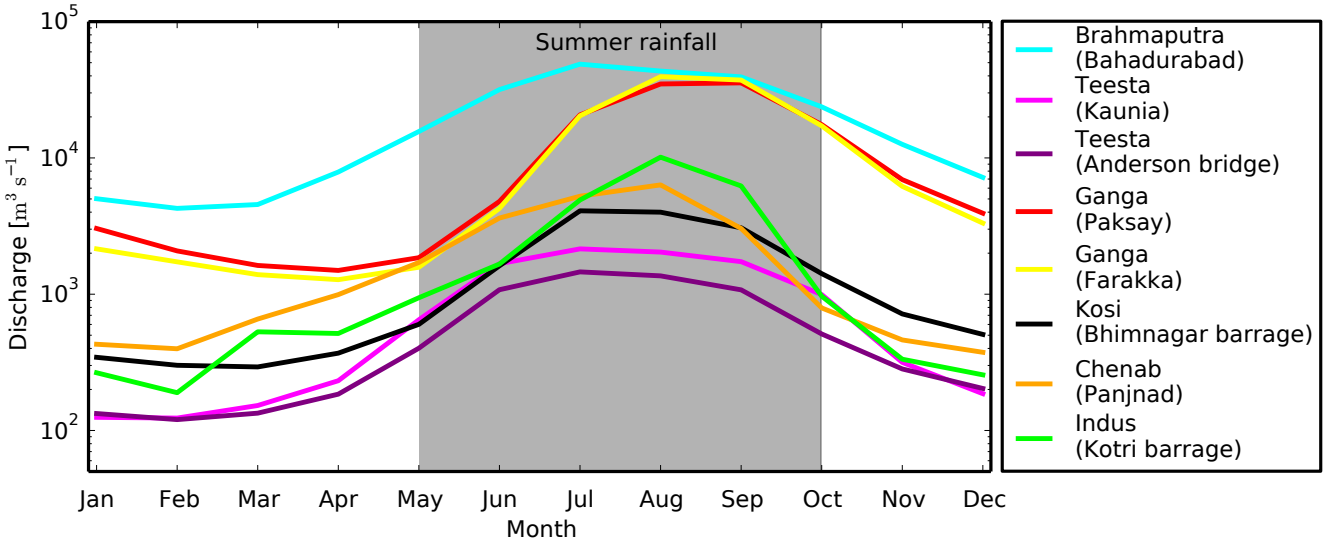

Figure 1. Hydrograph of the Himalayan Rivers

3 Morphology of alluvial river

Lacey (1930) was the first to observe a dependency of width of an alluvial river on its discharge. Based on measurements in various single-thread alluvial rivers and canals in India and Egypt, he found that the width of a river regime channel scales as the square root to the discharge ($e \sim 0.5$ in Eq. 1).

To explore the physical basis of Lacey's observation, Glover and Florey (1951) and Henderson (1963) developed a theory based on the concept of threshold channel. According to this theory, with a constant water discharge, the balance between gravity and fluid friction maintains the sediment at threshold of motion, everywhere on the bed surface. This mechanism sets the cross-section shape and size of a channel. The resulting width (W) - discharge (Q_w) relationship in dimensionless form reads (Seizilles, 2013; Gaurav et al., 2014; Métivier et al., 2016, 2017; Gaurav et al., 2017):

$$\frac{W}{d_s} = \left[\frac{\pi}{\mu}\left(\frac{\theta_t(\rho_s - \rho_f)}{\rho_f}\right)^{0.25}\sqrt{\frac{3C_f}{2^{3/2}\mathcal{K}[1/2]}}\right]Q_*^{0.5} \tag{4}$$

where $Q_* = Q_w/(d_s^2\sqrt{gd_s})$ is the dimensionless water discharge, d_s is the grain size, $\rho_f \approx 1000\,\mathrm{kg\,m^{-3}}$ is the density of water, $\rho_s \approx 2650\,\mathrm{kg\,m^{-3}}$ is the density of quartz, $g \approx 9.81\,\mathrm{m\,s^{-2}}$ is the acceleration of gravity, $C_f \approx 0.1$ is the Chézy friction factor, $\mu \approx 0.7$ is the Coulomb's coefficient of friction, $\mathcal{K}(1/2) \approx 1.85$ is the elliptic integral of the first kind, and θ_t is the threshold Shield's parameter that depends on the sediments grain size. The typical grain size of the sediments of the

Himalayan Foreland rivers is order of $d_s = 100 - 300\,\mu m$. Thus the dimensionless grain size $D^* = (d_s^3 g \rho_s^2/\eta^2)^{1/3} \simeq 1 - 6$, where $\eta \approx 10^{-3}$ Pa.s is the dynamic viscosity of water. In this range of values the threshold Shield number is on order of $\theta_t \sim 0.1$ with a maximum around 0.3 (Julien, 1995; Selim Yalin, 1992). Recently Delorme et al. (2017), obtained an experimental value of $\theta_t \sim 0.25$ for silica sands of size $150\,\mu m$. Here we have taken the upper value of $\theta_t = 0.3$ as a conservative estimate. Taking lower values of threshold Shield parameter, such as the classical 0.1 would lead to a slightly better match between the theoretical prediction and the data but it does not lead to a significant change in our conclusions.

Eq. 4 is the theoretical equivalent to the Lacey's law. This theory explains the mechanism how a single-thread alluvial river, at threshold of sediment transport, adjust their geometry in response to the imposed water discharge. Strictly speaking, mean equilibrium geometry of a natural alluvial channel is not set by a single discharge, rather a range of discharges is responsible for determining the channel form (Leopold and Maddock, 1953; Wolman and Miller, 1960; Blom et al., 2017; Dunne and Jerolmack, 2020). However, what value corresponds to the channel forming discharge of an alluvial river remains a matter of debate ~~?~~ Wolman and Miller (1960); Wolman and Leopold (1957); Phillips and Jerolmack (2016) proposed that the bankfull discharge and discharge associated with a certain frequency distribution can be used to define the channel forming discharge.

Since threshold theory predicts the ~~morphology~~ scaling relationship of a single-thread channel, one may ~~use it to estimate~~ consider applying it to assess the discharge that relates to present day geometry of natural alluvial channels. To test this, we use the regime curve that we established from threshold theory and measurement of hydraulic geometry of various sandy alluvial rivers in the Himalayan Foreland (Gaurav et al., 2014, 2017). In field campaigns during 2012, 2013, 2014, and 2018 we measured the geometry (width, depth, velocity and median grain size) of individual threads of braided and meandering river spanning over the Ganga and Brahmaputra plains. To measure the channel geometry we have used Acoustic Doppler Current Profiler (ADCP) on an inflatable motor boat. Close to the location of our ADCP-measured transects, we collected the sediment sample from the channel. We sieved the sediment sample in the laboratory to calculate the median grain size ($d_5 0$). A detailed descriptions of the measurement can be found in our previous publications (Gaurav et al., 2014, 2017).

Figure 2 suggests that the individual thread of the Himalayan Foreland rivers share a common width-discharge regime relation, and to the first order their morphology can be explained by threshold theory. The theoretical exponent accords with the empirical exponent of the width-discharge curve. However, the threads are wider than predicted by a factor of about 2 (Fig. 2). We ~~further~~ now adjust the prefactor ~~to the~~ predicted from threshold theory to our data while keeping the theoretical exponent to establish a generalised semi-empirical "width-discharge" regime relationship for the Himalayan Foreland rivers ~~.~~ ~~This regime curve is then used~~ (Fig.2). We then use this curve to estimate the discharge of various ~~Himalayan rivers~~ rivers of the Himalayan Foreland by measuring their width from satellite images.

4 Material and method

4.1 Dataset

To measure the width of a river channel, we use images acquired from Landsat Thematic Mapper (TM), Landsat 8 and Sentinel 1A satellites (Appendix A1). All images of the Landsat and Sentinel satellite missions are freely available and they can be

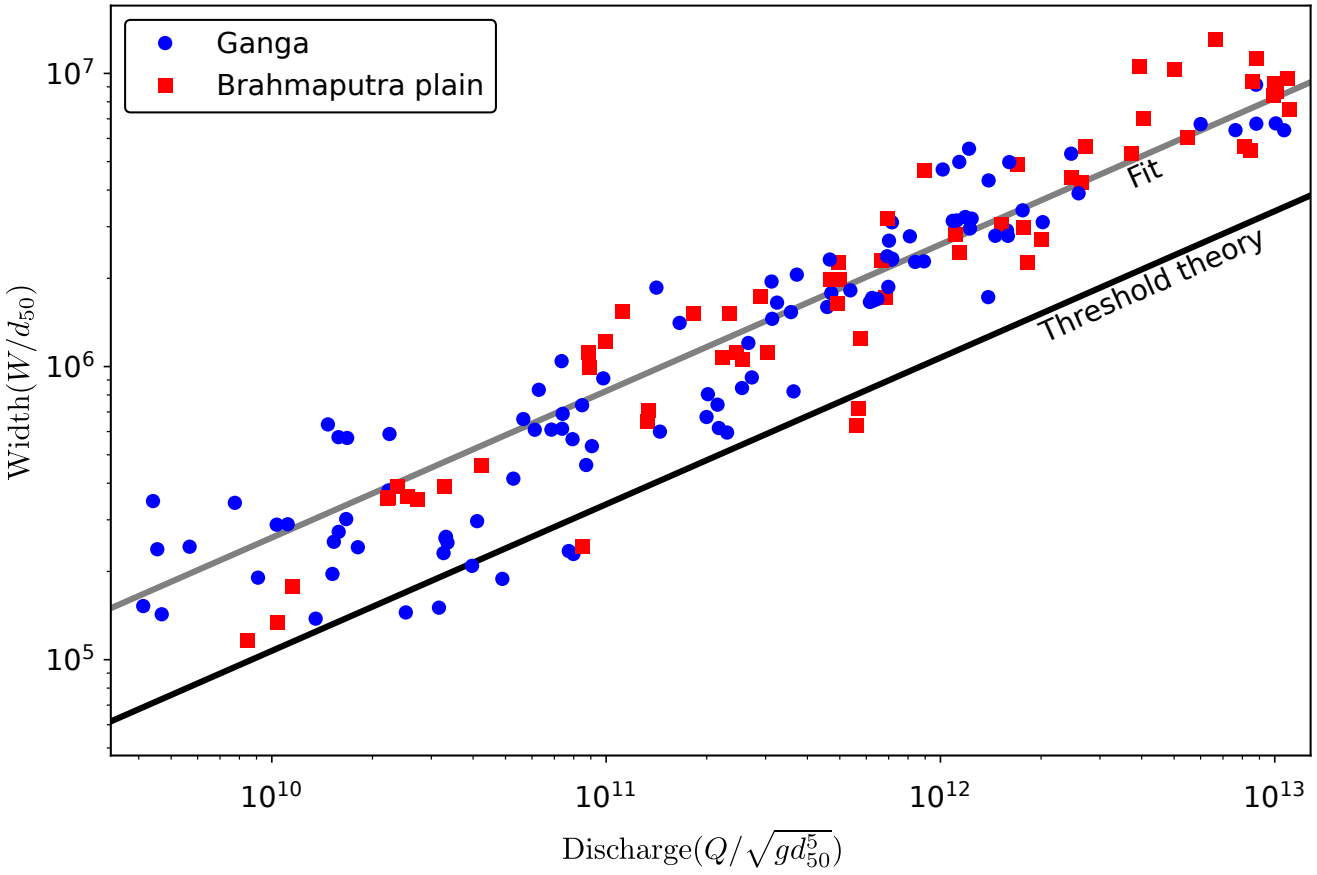

Figure 2. ~~Width~~ Dimensionless width of the individual threads of the Himalayan Foreland rivers as a function of dimensionless water discharge (after: Gaurav et al. (2017)). These data (width, discharge and grain size) were acquired during the different field campaign in years 2012, 2013, 2014 and 2018. The measurement was performed during the period when the Himalayan river usually flow at their formative discharge. The solid line (dark) is the prediction from threshold theory and the solid line (light) is obtained by fitting the prefactor of the threshold relation (Eq.4) to the data while keeping the theoretical exponent.

downloaded from the US Geological Survey (https://earthexplorer.usgs.gov) and Alaska Satellite Facility (https://www.asf.alaska.edu/sentinel) websites. We have downloaded all available cloud-free Landsat satellite images, at the locations that were near the in-situ measurement stations for which discharge data was available with us (Fig. 3). Only a few cloud free Landsat images are available for the period of June to September. This is mainly because of the strong monsoon that causes intense rainfall and dense cloud covers. To overcome seasonal effect and fill the data gap during the monsoon period, we use Sentinel 1A product. Sentinel-1 satellite mission is equipped with Advanced Synthetic Aperture Radar (ASAR) sensor that operates in C-band (5.4 GHz) of microwave frequency (Schlaffer et al., 2015; Martinis et al., 2018). Advanced Synthetic Aperture Radar

system can operate both day and night and has the capability to penetrate clouds and heavy rainfall. This special characteristic of SAR sensors enables uninterrupted imaging of the Earth's surface during the bad weather conditions as well.

In-situ measurements of average monthly discharge for some time intervals of varying length between 1949-1975 are available for the Brahmaputra, Teesta, Ganga, Chenab, and Indus rivers of the Himalayan Foreland. They can be freely downloaded from (http://www.rivdis.sr.unh.edu/maps). We could obtain discharge data for the period 1996 - 2005, for the Ganga River at Paksay station and the Brahmaputra River at Bahadurabad station from Bangladesh. Similarly, the Ganga River discharge from 1978 - 2007, measured at the Farakka station in India was obtained from the Central Water Commission, Ministry of Water resources, New Delhi. We also obtained discharge data for the Kosi River for the period 2002 - 2014, from the investigation and research division, Kosi project, Birpur and from our own field measurements (Appendix A2).

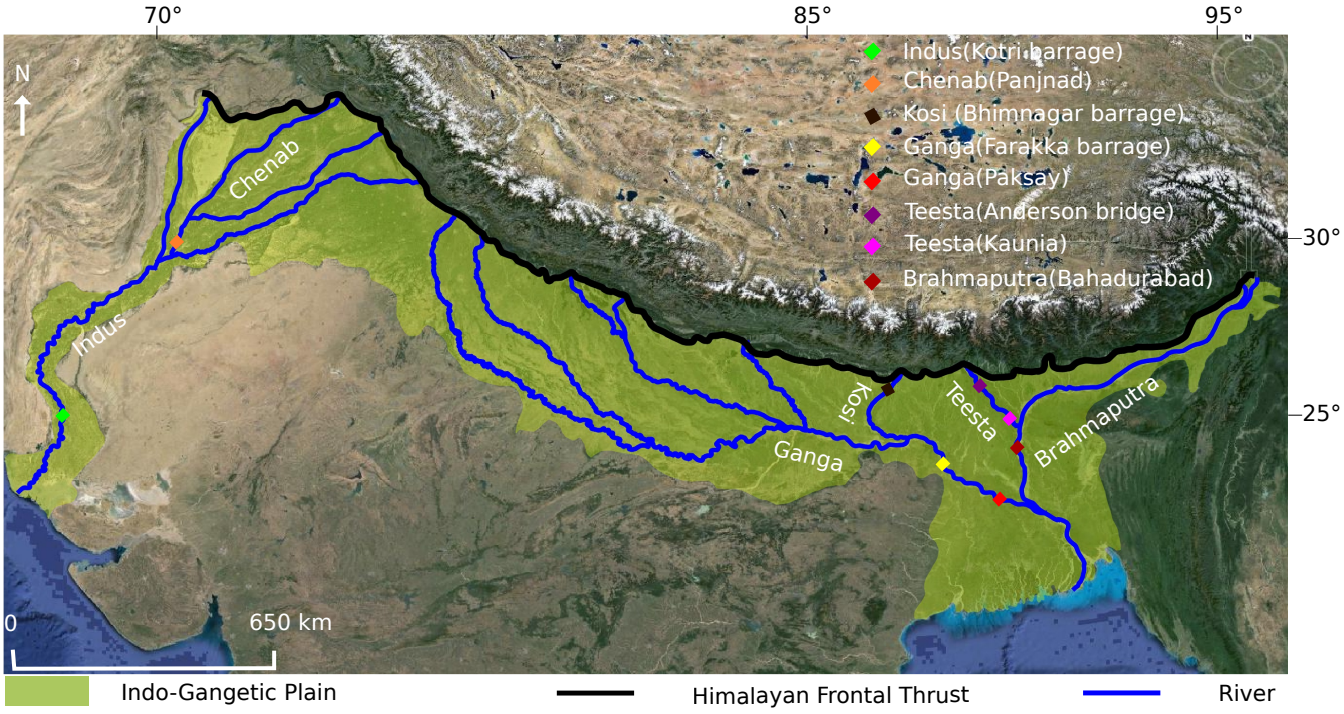

Figure 3. Location of the gauge stations of various rivers on the Indus, Ganga and Brahmaputra basins for which discharge data is available (source: https://www.google.com/earth/Google Earth).

4.2 Width extraction

Our main objective is to extract the width of individual river channels from satellite images. We have developed an automated program in python 3.7 that takes a gray scale image as an input to classify the image pixels into binary water and non-water classes. The pixels classified as water are the foreground object and will be used to define river channels. Dry pixels serve as a background object. To extract the river channels, we use the infra-red bands of Landsat-TM and Landsat-8 images. In

Landsat-TM, the infra-red ($0.76 - 0.90\,\mu$m) wavelength corresponds to band 4 whereas, in Landsat-8 image, it corresponds to band 5 ($0.85 - 0.88\,\mu$m). The spatial resolution of infra-red band for both Landsat- (TM & 8) missions is 30 m (pixel size: 30×30 m). Theoretically, since water absorbs most of the infra-red radiations it appears dark, with an associated brightness value close to 0. This typical characteristic of the infra-red signal allows a clear distinction between the water covered dry areas on the satellite images (Frazier et al., 2000). However, in the case of a river, the pixel intensity varies widely because of heterogeneous reflectance of river water, due to the presence of sediment and organic particles (Nykanen et al., 1998). Because the image intensity is not exactly 0 or 1, we introduce a threshold intensity to classify the pixels. Based on this criteria, we convert the gray scale image $f(x,y)$ into a binary image $g(x,y)$, which distinguished between the water-covered and dry areas. This approach takes an object-background image and selects a threshold value that segments image pixels into either object (1) or background (0) (Ridler and Calvard, 1978; Sezgin et al., 2004).

$$g(x,y) = \begin{cases} 0, & \text{if } f(x,y) < T \\ 1, & \text{if } f(x,y) >= T \end{cases} \tag{5}$$

We apply the algorithm proposed by Yanni and Horne (1994) to obtain the threshold value iteratively. Once this optimal value is obtained, we apply it to classify our pixels into water and dry classes (Fig. 4). The binary classification of satellite images into water and dry pixels can produce spurious features as well (Fig. 4). These consist of wet pixels that get classified as dry or of isolated water pixels that appear randomly in the binary images (Passalacqua et al., 2013). Clusters (usually 2-3 pixels in size) that appear inside the river network do not correspond to bars or islands. We found frequent areas where strong reflection from the bed sediment cause water pixels to appear more like sand. Isolated water pixels that do not belong to the river are located in water-logged areas. We identify these types of errors and reprocess the binary images to remove them automatically. For this, we first identify the isolated water patches from the binary images. To do this, we define a search window of 7×7 pixel size. We run this window on the image and look for neighboring water pixels in all surrounding directions. If a water pixel in the classified image is disconnected in all directions from the neighboring water pixels for more than seven pixels, we consider them as isolated water bodies. We therefore re-classify such pixels as dry. We re-iterate this procedure by applying a region growing algorithm (Mehnert and Jackway, 1997; Bernander et al., 2013; Fan et al., 2005). For this we initially select a water seed pixel inside the river channel. The algorithm uses the initial water pixels and starts growing. This procedure removes all isolated water patches from the binary image, and retains only water pixels connected to the river network.

Once images are reclassified, we reprocess them to merge the water pixels that were initially classified as dry inside a river channel. For this we define a search window of 3×3 pixels. We choose this size by assuming that dry pixels should be more than 90 meter in size to be considered as bars or islands. Otherwise, such pixels are treated as water pixels. We move the search window on the binary image and look for neighboring dry pixels inside the river channel.

Similarly, to identify river pixels from Sentinel 1A images, we use VH (Vertical transmission and Horizontal reception) polarized band. We have Sentinel Application Platform (SNAP) v6.0 to perform the radiometric calibration, speckle noise reduction using refined Lee filter and terrain corrections and finally generate the backscatter (σ_0) image. This image has pixel

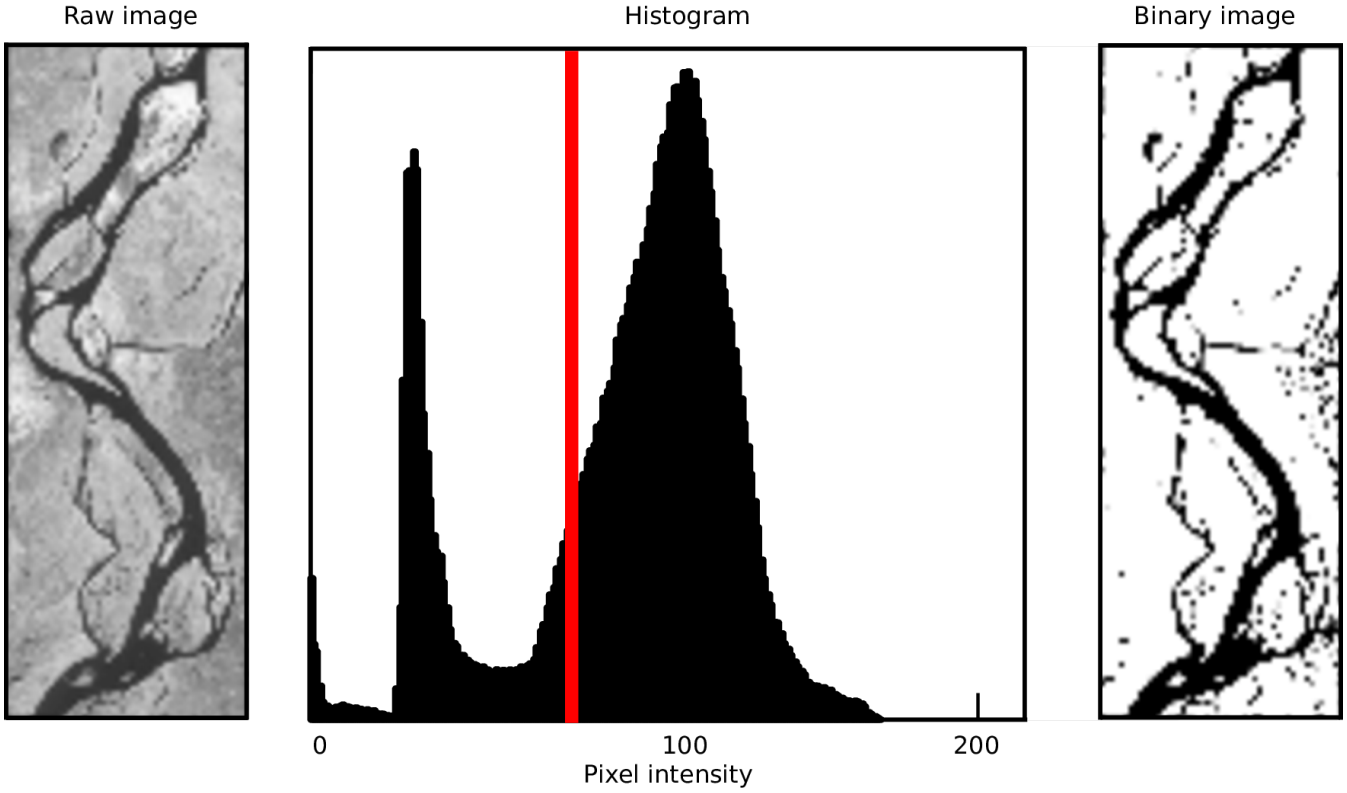

Figure 4. Histogram showing the distribution of pixel gray level intensity values. The optimal threshold (T) value (marked with red line) is obtained from the iterative threshold selection algorithm.

size of $60 \times 60m$ that we resampled at $30 \times 30m$ to be consistent with the pixel size of Landsat images. In microwave region, open and calm water bodies exhibit low backscatter values due to high specular reflection from the water surface (Schlaffer et al., 2015; Twele et al., 2016; Amitrano et al., 2018). We manually set a threshold value to separate water and dry pixels from Sentinel-1 images. Finally, we follow a similar procedure as we developed for Landsat images to process the binary image obtained from Sentinel-1.

Once the satellite images are classified, we use the binary images to extract the width of each channel. We do this by measuring the distance from the center of a channel to its banks orthogonally to the flow direction. A detailed automated procedure of width extraction of a river channel is given in Appendix B.

5 Result

5.1 Accuracy assessment

To assess the precision with which we can estimate the discharge of a thread, we need to quantify the accuracy of our width-extraction procedure using Landsat and Sentinel-1 satellite images. To evaluate this, we superimpose the contours of river channels, extracted using our algorithm, to the original gray-scale images used for the extraction. We then carefully check for a match between the contours boundary and water boundary in gray scale image. We observed a good agreement between automatically extracted channel boundary and the edge of the water line in gray image. However, our algorithm fails to extract the contours of the smallest channels (60 - 90 meter in width). Several reasons explain this limitation. First, as these channels are both shallow and only a few pixels wide, their pixel intensity is close to the pixel intensity of dry areas. Therefore, the optimal threshold applied to categorize the image pixels does not identify these channels as water. Second, although an increase in the classification threshold could force the algorithm to identify these pixels as water, it would also add significant noise by classifying many dry pixels as water pixels. Such a limitation appears to be closely related to the image resolution.

Given this qualitative agreement, we proceed to evaluate the accuracy of the width extraction procedure. To do this, we overlay the transects used by the algorithm to measure the width of a thread on the original image (Fig. 5 a). We then manually measure the width at randomly selected transects for comparison. For each river, we manually measure the width at more than 15 randomly selected transects. We then compare the automatically extracted and manually measured widths.

Figure 6 compares the widths extracted automatically and manually. Most of the data points cluster on the 1:1 line. This indicates that, for the vast majority of threads, the width computed from our automated procedure is almost equal to the width measured manually.

There are some outliers however. They correspond to places along the threads where our automated procedure draws erroneous transects (Fig. 5 b). Most of such transects are located near highly curved reaches at the confluence or diffluence of two or more threads. In such places, the width of a thread is overestimated sometimes by more than $50\,\%$ compared to the width measured manually. At most locations though, our procedure extracts valid transects (Fig. 5 a).

Further, we assess the distribution of relative discrepancies between automatically and manually measured widths (Fig. 7). To quantify the precision of our measurement we compute the relative error. We observe that the relative error of $90\,\%$ of our measurements is centered around a mean $\mu \approx -0.02$ with a standard deviation $\sigma \approx 0.07$. This validates the width-extraction procedure.

5.2 Width variability along a thread

Particularly in a braided river, the width of a thread varies significantly along its course. To quantify this variability, we select a reach and plot the probability distribution of the width measured across different transects. We observed that the distribution of width histograms is skewed Figure 8. This skewness results from the natural variability of width along the course and also due to the error in width extraction from images, particularly at the location where the curvature of a thread is high. The resulting skewness will be amplified in the discharge histogram because of the non-linear relationship relating the two variables. To take

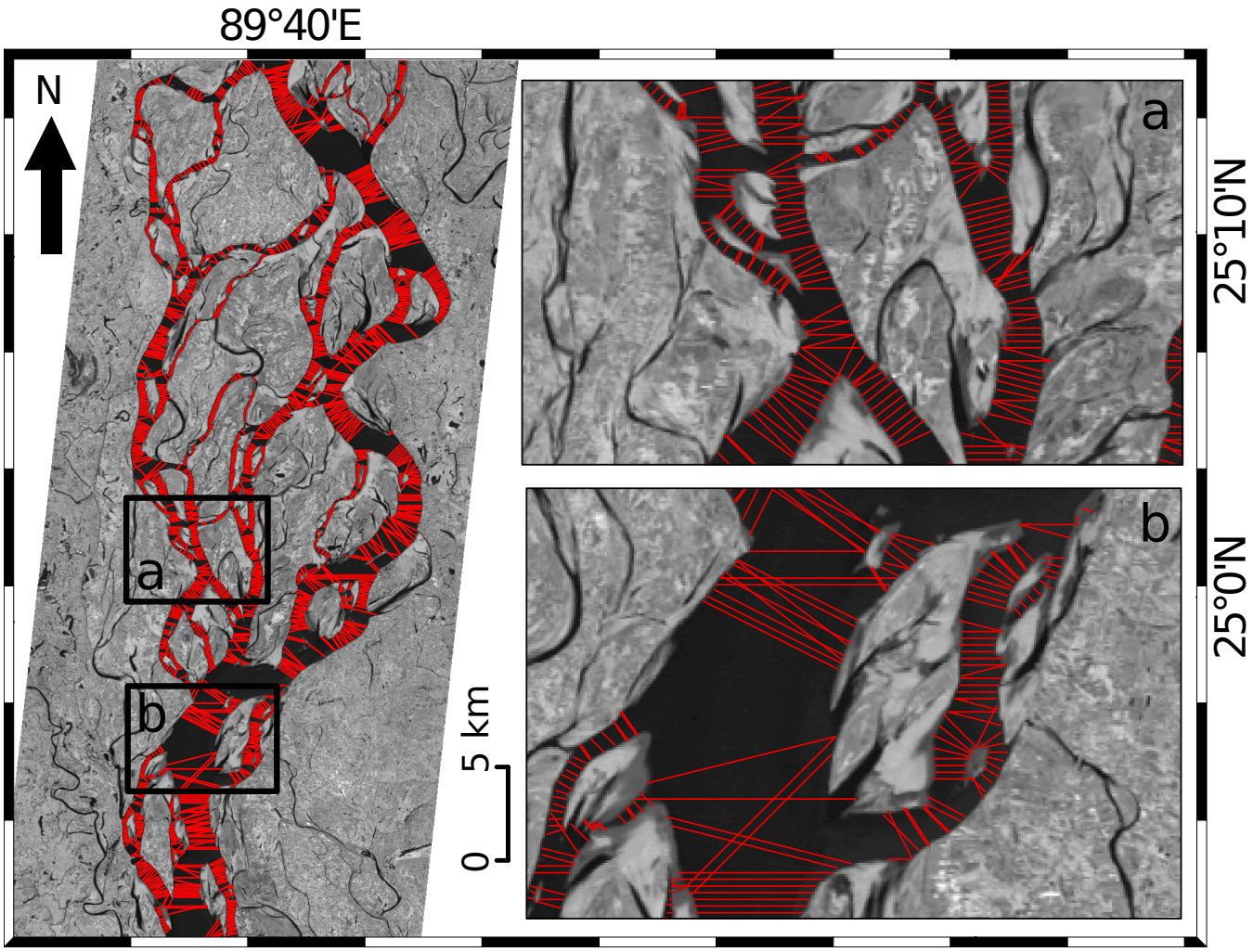

Figure 5. Width of the individual threads estimated across different transects along a reach of the Brahmaputra river from Landsat satellite image. Windows (a) and (b) illustrate the regions of valid and erroneous transects at different places in the river (image source: Landsat-TM, 29 November 2013).

the skewness into account, we have ~~used the most probable width W_m as the representative value of the width (Eq. 1). This value corresponds to the~~ calculated the geometric mean of all the measured values. The geometric mean is less affected by extreme values in a skewed distribution and can be considered a representative width (W_r). However, in meandering rivers where the variability in width within a reach is not much, arithmetic mean can be considered a representative width.

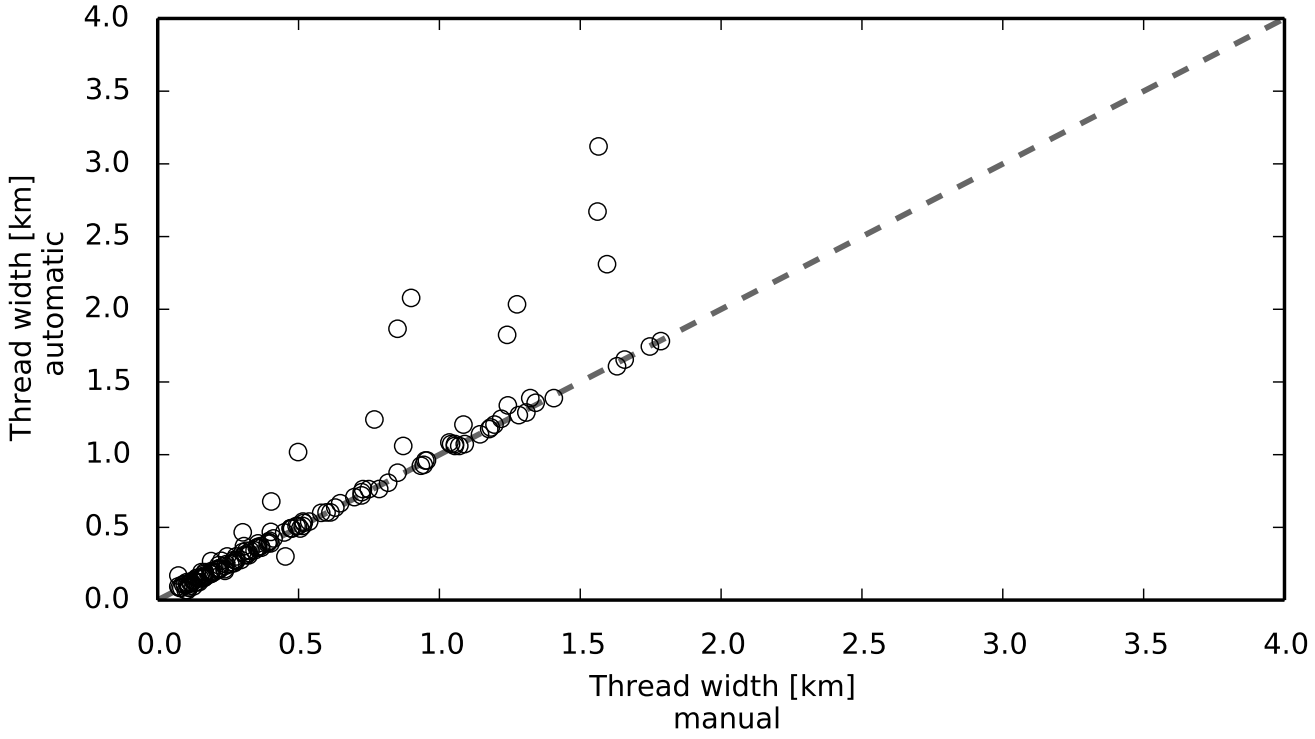

Figure 6. Threads width extracted using automated technique is plotted as function of width extracted manually.

5.3 Discharge estimation

We now proceed to estimate discharge (Q_w) for the Himalayan Rivers based on their channel widths ~~measured~~ extracted from satellite images. To have a meaningful comparison between the image derived discharge and the corresponding in-situ measurement, we select a reach about ten times longer than the width of a river on satellite images. In the case of a braided river, we consider the widest channel to define reach length. In the selected reach we assume that discharge is conserved, there is no significant addition or extraction of water in the river.

To estimate discharge of the study reach, we use a regime relation established by Gaurav et al. (2017) based on threshold channel theory (Eq. 4) and field measurements of channel's width and discharge on the Ganga-Brahmaputra Plain. The resulting regime relation is governed by:

$$Q_w = \left(\frac{W_m}{\alpha}\frac{W_r}{\alpha}\right)^2 \sqrt{\left(gd_s \cdot \sqrt{(gd_s)}\right)}, \tag{6}$$

where α is the best-fit coefficient, an empirical value obtained from fitting the prefactor of the regime curve (Eq.4), W_r is the representative width and ~~W_m is the most probable width~~ d_s is the median grain size.

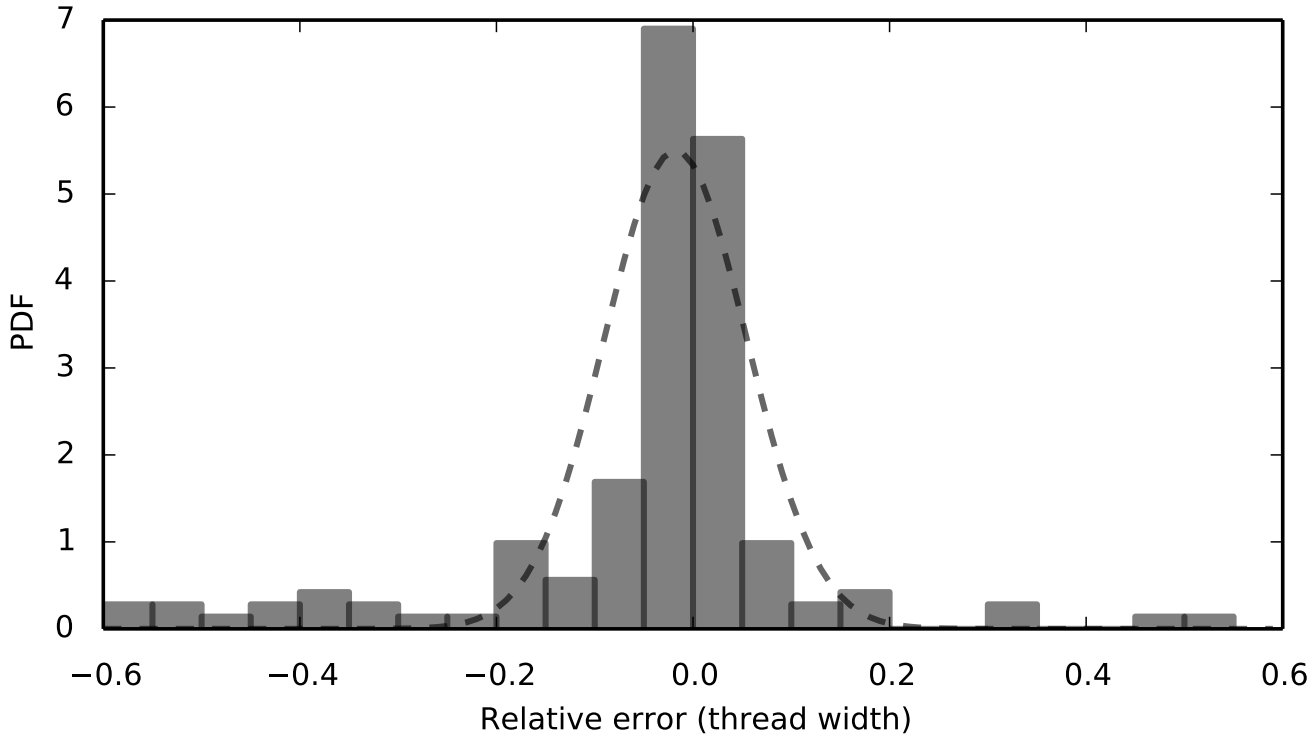

Figure 7. Distribution of the error in the threads width extracted automatically. The corresponding normal distribution is obtained by removing the 10 % extreme values from the distribution.

We use Eq. 6 to calculate the discharge for threads of known width. Because the river width scales non-linearly with discharge, regime relations obtained refer to the total width in the case of a braided river; and will not be the same as those obtained for individual threads. Since most of the studied rivers are braided, we first calculate the discharge for individual threads across a given section. We then sum the discharge of the individual threads across a transect to compute the total discharge at a section.

5.4 Estimated Vs. measured discharge

Once monthly discharges for all the rivers are estimated from satellite images, we compare them with the average monthly discharge measured at the corresponding gauge stations. To do so, we plot the hydrographs of the estimated and measured discharges together (Fig. 9). We ~~observe~~ observed that the estimated discharge of the Kosi, Ganga, and Brahmaputra rivers from satellite images ~~remains constant throughout the year, except during the monsoon period (June-September)when all the~~ is overestimated and almost constant throughout during the non-monsoon period (October-May). Conversely, the Indus, Chenab, and Teesta rivers show a ~~significant rise. During the non-monsoon period (October-May), estimated discharges~~ clear annual

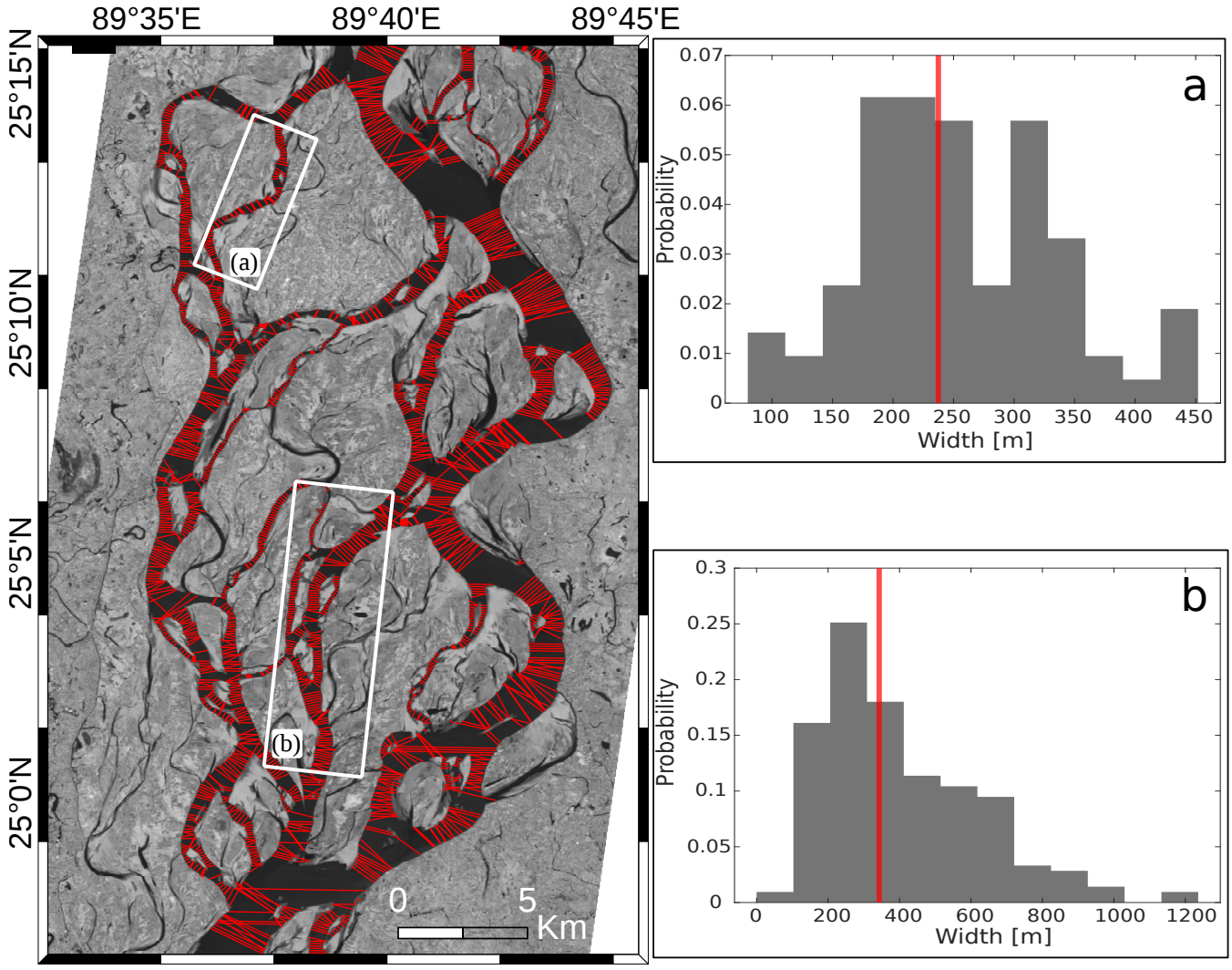

Figure 8. Spatial distribution of the width measured along threads of a braided reach of the Ganga River near the Paksay Gauge station in Bangladesh. Vertical line (red) on the histograms (a and b) is the geometric mean that corresponds to the most probable width (Wm).

cycle. This observed trend is not entirely clear to us, it could possibly be related to the flow regulation, as these river are highly regulated through a series of dams and barrages.

Further we observed that the estimated discharge for most of our rivers ~~are overestimated~~show a significant rise during the monsoon period (June-September). To the first order, it appears that our approach is able to capture the rising trend of discharges during the monsoon period, however the estimated discharges are lesser than the measured discharges. Table 2 compares the estimated and measured discharges during the monsoon period. For most of our rivers, the difference between

measured and estimated discharges are less than 50%; though this difference is comparatively high for the Indus ($72-78\%$) and Chenab ($36-67\%$) rivers (Table 2).

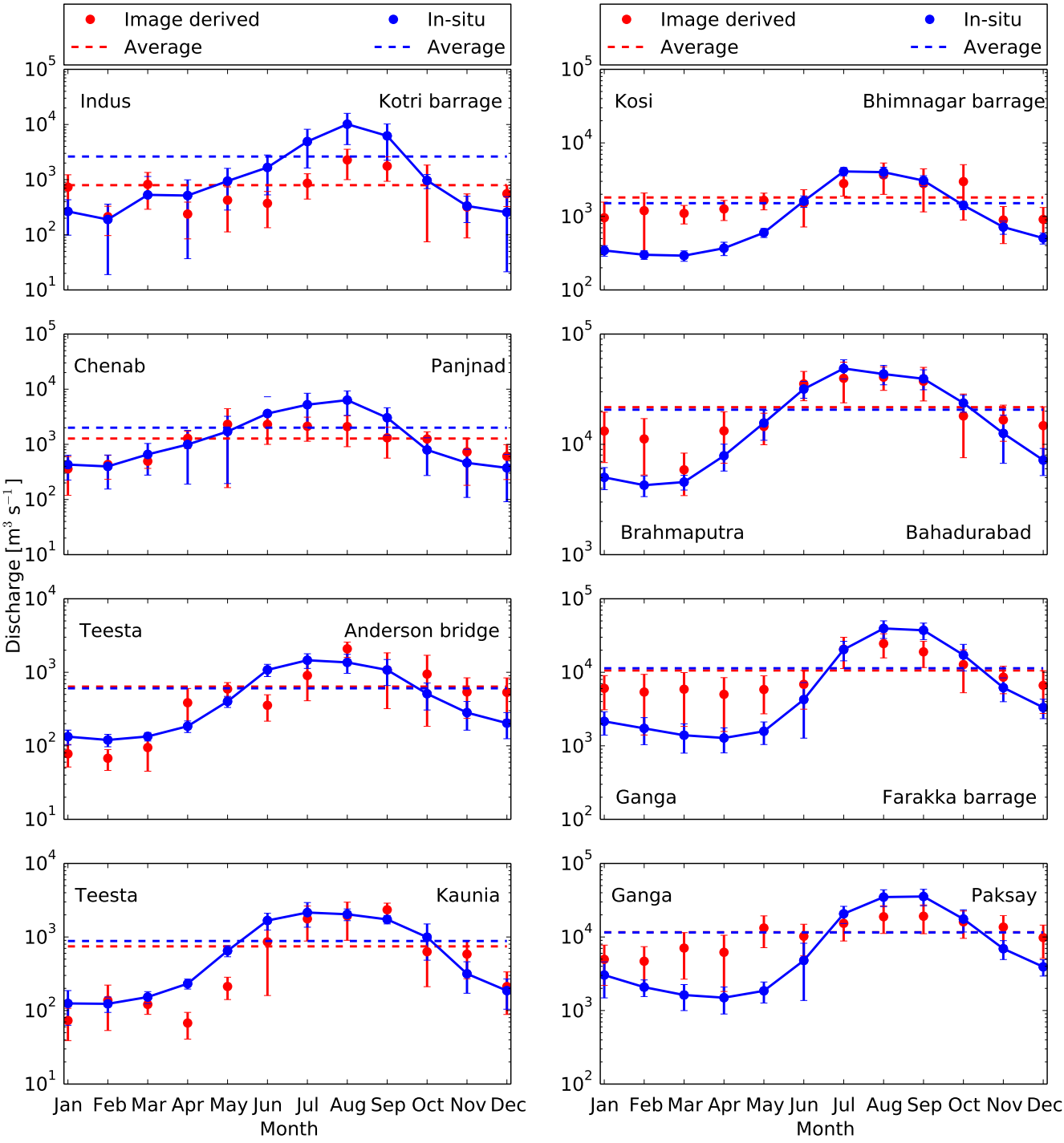

Figure 9. Hydrograph of satellite derived ~~river~~ reach averaged discharge against their monthly average discharge recorded at the gauging station. Error bar in measured discharge (blue) is the standard deviation calculated from the time series of different month. Error bar in estimated discharge represents the standard deviation within the study reach. Dotted red and blue lines are the annual average discharge obtained from satellite images and in-situ measurement respectively.

Rivers		Monsoon discharge $[m^3 s^{-1}]$ Jun	Jul	Aug	Sept
Kosi (Bhimnagar barrage)	In-situ	1616 ± 285	4091 ± 530	3998 ± 660	3072 ± 509
	Image derived	1515 ± 797	2800 ± 912	3660 ± 1667	2796 ± 1644
	Difference (%)	-6	-32	-8	-9
Brahmaputra (Bahadurabad)	In-situ	31717 ± 5536	48769 ± 9640	43387 ± 8722	39320 ± 8071
	Image derived	35335 ± 10491	39716 ± 15914	40653 ± 9808	37316 ± 12580
	Difference (%)	11	-19	-6	-5
Ganga (Farakka barrage)	In-situ	4260 ± 2989	20375 ± 6059	39462 ± 10665	37264 ± 9415
	Image derived	6864 ± 3717	20599 ± 9343	24562 ± 8871	18971 ± 7364
	Difference (%)	61	1	-38	-49
Ganga (Paksay)	In-situ	4794 ± 3425	20691 ± 5427	34887 ± 9002	35546 ± 8985
	Image derived	10226 ± 4689	15333 ± 6510	18862 ± 7691	19168 ± 8089
	Difference	113	-26	-46	-46
Teesta (Anderson bridge)	In-situ	1078 ± 204	1458 ± 330	1363 ± 395	1076 ± 416
	Image derived	356 ± 139	904 ± 494	2086 ± 494	1079 ± 759
	Difference (%)	-67	-38	53	0
Teesta (Kaunia)	In-situ	1674 ± 428	2151 ± 792	2037 ± 369	1733 ± 227
	Image derived	860 ± 700	1765 ± 883	1938 ± 1036	2346 ± 540
	Difference (%)	-49	-18	-5	35
Indus (Kotri barrage)	In-situ	1665 ± 1136	4912 ± 3290	10128 ± 5807	6227 ± 3980
	Image derived	372 ± 238	861 ± 417	2279 ± 1279	1759 ± 826
	Difference (%)	-78	-82	-77	-72
Chenab (Panjnad)	In-situ	3621 ± 2812	5235 ± 3206	6340 ± 2983	3038 ± 1574
	Image derived	2300 ± 1302	2125 ± 988	2099 ± 1193	1311 ± 749
	Difference (%)	-36	-59	-67	-57

Table 1. Comparison between the image derived and in-situ measured discharge of the Himalayan rivers during the Indian summer monsoon period. Error in measured discharge is the standard deviation calculated from the time series of different month. Error in estimated discharge is the standard deviation within the study reach.

6 Discussion

It is important to note that the discharge estimated from satellite images does not correspond to an instantaneous discharge. To understand the emergence of constant hydrograph from the estimated discharge derived from satellite images we explore the concept of channel forming (formative) discharge i.e. a discharge that sets the geometry of alluvial river channels. Several workers Inglis and Lacey (1947); Leopold and Maddock (1953); Blench (1957), have shown that the geometry of an alluvial channel corresponds to a formative discharge (see table A3 in appendix for the definition of different discharges). They have discussed how a limited range of flows are responsible for shaping its channel. At low-flow discharge, the water simply flows through the threads without affecting their geometry. Schumm and Lichty (1965) used the concept of time span (geologic, modern and present) in defining the interrelationship between dependent and independent variables of a river system. According to them, morphology of a river channel is set in the modern time span (last 1000 years) by the average discharge of water and sediment. In the present time span (1 year or less), channel morphology can be considered as independent variable against instantaneous discharge of water and sediment.

Similarly, it has been argued by Inglis and Lacey (1947); Leopold and Maddock (1953); Blench (1957) that it is not the highest flows that contribute the most in shaping a river channel. Such high discharges are capable of transforming the channel, but they occur so infrequently that, on average, their morphological impact is small. Wolman and Miller (1960) highlighted that the bankfull discharge that occurs once each year or every two years sets the pattern and channel width of the alluvial rivers. Formative discharge for the Himalayan rivers is expected to occur in the monsoon period, thus one may expect that during low flow such rivers maintain their flows without modifying the existing channel geometry (Roy and Sinha, 2014). This clearly reflects in the discharge hydrographs estimated from the measurement of channel's width from the satellite images (Fig. 9. Furthermore, Métivier et al. (2017) have recently shown that non cohesive streams laden with sediments cannot have a width much larger than the width of a threshold stream before they start to braid. They also showed that, for experimental braided rivers, threads are always formed at the bankfull flow, and at the limit of stability. Our hypothesis is thus that the formative discharge of threads in the Ganga plain is the bankfull discharge." This is probably why for most of the rivers our estimated discharge from satellite images remain constant throughout during the non-monsoon period and is mostly overestimated than the measured discharge at gauge stations.

According to Inglis and Lacey (1947), rivers approach their equilibrium geometry for a formative discharge that approximately corresponds to the bankfull discharge. They suggested this discharge lies between 1/2 and 2/3 of the maximum discharge. It has also been suggested that the formative discharge corresponds to the median discharge (Blench, 1957). In their study, Leopold and Maddock (1953) used the discharge that corresponds to a given frequency of occurrence and compared it to the hydraulic geometry of the river. Based on their observations in the United States, they recommended the use of the annual average discharge as a proxy for the formative discharge. Hereafter, we use the definition of Leopold and Maddock (1953).

Based on our understanding of the geometry of alluvial river channels, we argue that the width of the thread that we extract from satellite images corresponds to a formative discharge. ~~Therefore~~ As discussed by Gaurav et al. (2014), high-resolution bathymetry profile of a braided thread reveals complex topography of the bed. Flow within the thread is separated by submerged

bars and islands. In such situations, discharge is not carried across the width seen from the plan view, but only through the narrow active regions. Further, this indicates that during the low flow water spread in the existing geometry set at the formative discharge. Currently, satellite images allow us to measure the top width of the water surface. We presume for a given ~~river~~thread, discharge estimated from these widths should compare with the formative discharge.

We now evaluate how the discharge estimated from satellite data varies with time. We plot the monthly discharge estimated for all of our rivers to their corresponding average monthly discharge measured at the gauge stations (Fig. 9). The monthly average discharge of the Himalayan Foreland rivers appears to be a representative of the actual hydrograph (Fig. C1). As suggested earlier by Inglis and Lacey (1947); Leopold and Maddock (1953) and Blench (1957) we observe that ~~the~~ except for the Indus, Chenab, and Teesta river, the estimated discharges from images are nearly constant throughout ~~the year, with only~~ during the non-monsoon period, with small fluctuations around their mean. This supports the hypothesis that the width of the thread extracted from satellite images corresponds to a ~~formative discharge.~~

~~Now we compare the discharge estimated from satellite images to the discharge measured at a nearby gauging station. To do this, we first~~ value closer to the formative discharge.

To go further, now we compare the annual average discharge estimated from Landsat and Sentinel-1A images for different months to the annual average discharge measured at corresponding ground stations. We plot these discharges on a log-log scale (Fig. 10). The discharge estimated from satellite images agrees to an order of magnitude with the measured discharge.

The difference between measured and estimated annual average discharges for the Brahmaputra, Ganga, Kosi, and Teesta rivers is less than $20\,\%$. However, this difference is comparatively high for the Indus ($78\,\%$) and Chenab ($49\,\%$) rivers. Interestingly, the estimated discharge for the Teesta (at Anderson station), Ganga (at Farakka & Paksay) and Brahmaputra (at Bahadurabad) rivers converge to their measured discharge with a small difference of $5\,\%$, $8\,\%$, $4\,\%$ and $< 1\,\%$, respectively (table 2); whereas the estimated discharge of the Teesta (at Kaunia station) and Kosi (at Bhimnagar) show a relatively higher difference of $19\,\%$, and $16\,\%$. This difference could be possibly related to the anthropogenic impact on the natural flow condition. For example, the selected study reaches for the Teesta (at Kaunia station) and Kosi (at Bhimnagar) rivers is located near the barrage where flow is ~~highly~~ regulated. However, this relationship is not entirely clear at this stage.

Similarly, the observed annual cycle in discharge and large difference between the estimated and measured discharge of the Indus and Chenab rivers could possibly be related to a series of dams and barrages (Kotri barrage, 1955, Mangla dam, 1967, Tarbela dam, 1976) that have been constructed. Such interventions have significantly altered the water and sediment discharge of the Indus river. For example, downstream of the Kotri barrage, the average annual water discharge of the Indus river has declined at an alarming rate of about (107 to 10) $\times 10^9\,\mathrm{m}^3$ from 1954 to 2003 (Inam et al., 2007). This continuous decline in the average annual discharge might have significantly modified the geometry of the Indus river.

Further to understand our estimates of discharge for the Chenab, Indus and Teesta rivers, we plot their monthly discharge time series recorded at the corresponding gauge station together with the discharge estimated from satellite images (Fig. C2 and C3). Despite a large variability, the discharge time series of Indus and Chenab rivers show a strong declining trend during the monsoon period (June-September); whereas discharge during the non-monsoon period appears to remain constant around the mean value. Figure (C2) clearly show that discharge estimated from satellite images plot within the variability of the observed

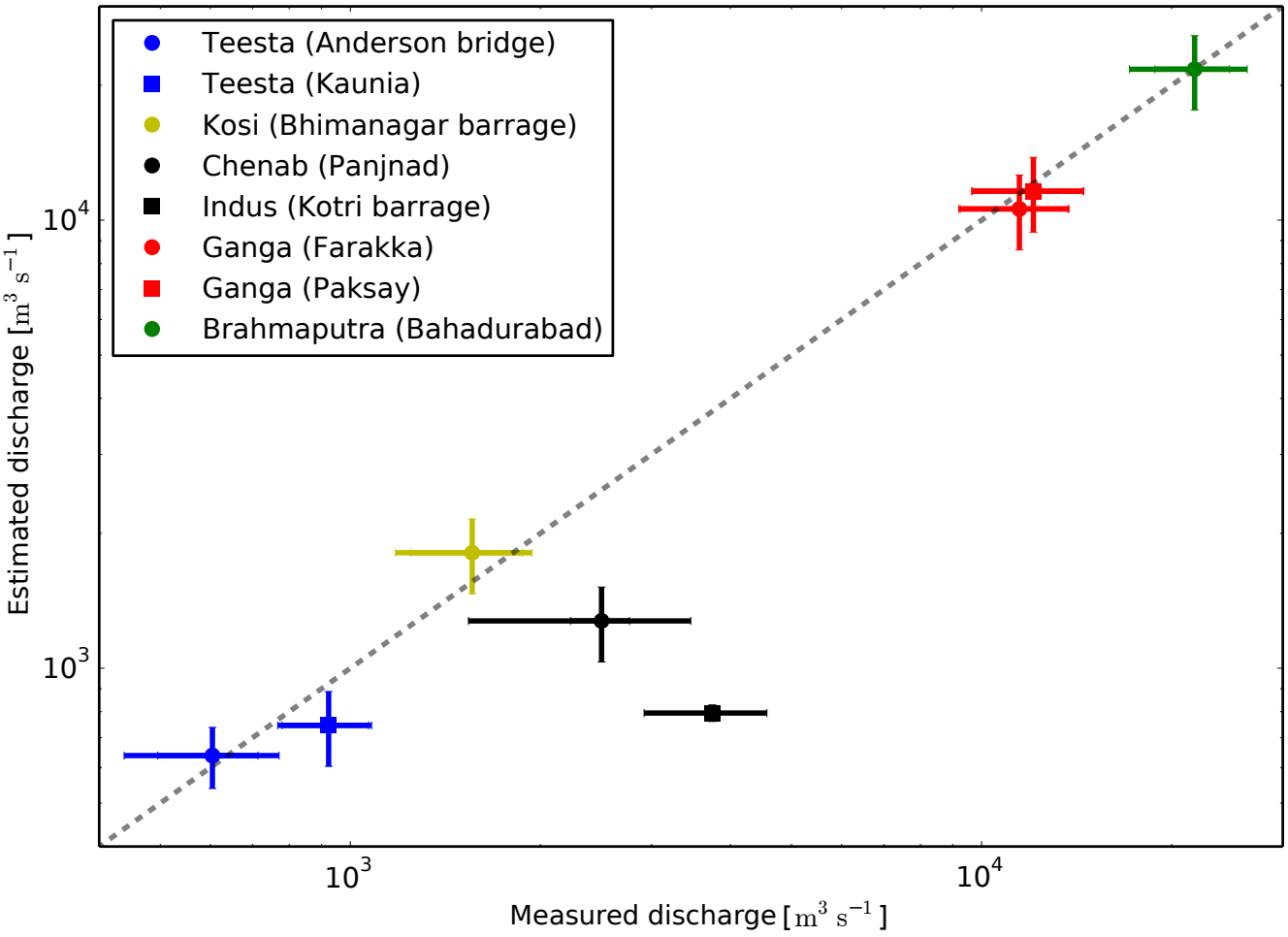

Figure 10. Satellite-derived river discharge against annual average discharge measured at a ground station. Error bar in measured discharge represent the standard deviation. Error bar for estimated discharge is calculated by considering $\pm 10\%$ measurement uncertainty in the channels width from satellite images.

trend. The estimated discharge of the Teesta River also plot within the noise of the observed trend. This gives a confidence in our estimates of discharge, especially for the rivers we have the limited and old record (1973-1979) of in-situ discharges.

In a recent study Allen and Pavelsky (2018) measured the width of the global rivers from Landsat images for the month when they commonly flow near mean discharge. We have used the water mask binary images from "Global River Width from Landsat (GRWL) database" and measure the threads width of the Brahmaputra, Chenab, Ganga, Indus and Teesta rivers (Appendix C). We used these widths to estimate discharges using our regime curve and compare them with the mean annual discharge recorded at the corresponding gauge station and our estimates from satellite images. We observed for most of our rivers the discharge estimated from thread's width extracted from the GRWL database of Allen and Pavelsky (2018) falls within

River	Station	$\langle Q_{insitu} \rangle$ m^3s^{-1}	$\langle Q_{sat.} \rangle$ m^3s^{-1}	$Q_{diff.}$ m^3s^{-1}	$Q_{diff.}$ %
Teesta	Anderson	605 ± 109	638 ± 165	33	5
Teesta	Kaunia	924 ± 144	745 ± 155	-179	19
Kosi	Bhimnagar	1559 ± 313	1810 ± 380	251	16
Chenab	Panjnad	2500 ± 961	1275 ± 268	-1225	49
Indus	Kotri	3745 ± 825	794 ± 162	-2951	78
Ganga	Farakka	11477 ± 2279	10593 ± 2225	-884	8
Ganga	Paksay	12080 ± 2403	11605 ± 2438	-475	4
Brahmaputra	Bahadurabad	21751 ± 2942	21717 ± 4740	-34	< 1

Table 2. Comparison between the annual average discharge measured at the gauge stations and estimated from satellite images.

the same order of magnitude to the yearly average discharge measured at the corresponding gauge stations (Table C1). ~~This suggests that water mask from GRWL database can be used as~~ For most rivers, the difference between measured and estimated discharge from GRWL data are approximately less than 60%. However this difference is comparatively high for the Kosi (88%) and Indus (95%) river. Interestingly, in accordance to estimates, GRWL database also show a high reduction in discharge of the Indus and Chenab river from the measured discharge at their corresponding ground stations during the period 1973-1979.

The GRWL database is a first ever compilation of width for the global rivers, it may be used together with our regime curve to obtain a first order approximation of ~~the mean~~ formative discharge of the Himalayan Foreland rivers. ~~Also we noticed that the discharge estimated from GRWL database appears to occur during early (June, July) or post (September, October) monsoon period.~~

7 Conclusion and future outlook

The semi-empirical regime relation established by Gaurav et al. (2017) and remote sensing images can be used to obtain a first order estimate of the formative discharge of ~~any river in~~ the Himalayan Foreland, if their channel width is known. The regime equation used here is established from the recent measurements and the published data by Gaurav et al. (2014, 2017) . This equation is based on threshold theory and instantaneous measurements of hydraulic geometry of individual threads of various braided and meandering rivers. ~~These~~ The measurements were acquired during the period when rivers of the Himalayan Foreland usually flow at their formative discharge (Roy and Sinha, 2014). Therefore, this regime equation only provides an estimate of the formative discharge, and it can not capture the instantaneous variations of discharge. On the other hand, as this regime relation is established from the measurements in braided and meandering rivers, it can be used to estimate ~~the~~ first order estimate for formative discharge in a river of any planform. It is especially useful and relevant for braided rivers that present several difficulties for the measurement of discharge in the field. Our regime equation requires only one parameter (grain-size) to estimate discharge from width measurements. It can be obtained easily from field measurements in the field. Since

our regime equation is established from measurement of a wide range of channels spanning over the Ganga and Brahmaputra plains, we believe it can be used to obtain the first order estimate of formative discharge of rivers in the Himalayan Foreland by just measuring their channel width on satellite or aerial images.

Using our semi-empirical regime equation and satellite images of Landsat and sentinel-1 missions, we have estimated the discharge of six major rivers in the Himalayan Foreland (Brahmaputra, Chenab, Ganga, Indus, Kosi, and Teesta). Our estimated discharges closely compare with the average annual discharge measured at the nearest gauging stations. This first-order agreement although encouraging, requires further research to improve the degree of agreement between measured and estimated discharges. One of the main source of uncertainty in discharge estimate is due to the error in the measurement of thread's width. This depends on the image resolution and accuracy of the algorithm used for extraction of river pixels from remote sensing images. A better resolution remote sensing images would most likely minimise the uncertainty and improve the agreement between estimated and in-situ discharge. Further our regime equation established for Himalayan rivers is based on a simple physical mechanism that explains the geometry of alluvial channels. We therefore suspect that the procedure we have established could be extended to most alluvial rivers. Globally it has been observed that the threshold theory well predicts the exponent of the regime equation (Eq. 6), however the prefactor may vary significantly depending on the grain size distribution, turbulent friction coefficient and the critical shield parameter (Métivier et al., 2017). It is therefore suggested to modify this regime curve from the measurement of width, discharge and grain size of a individual threads of alluvial channels in the field before applying it to the rivers of different climatic regime. Further it should be noted that our regime curve relates to the measurement of hydraulic geometry of individual threads of braided and meandering rivers, therefore it is applicable only at the thread scale. Since the resulting regime curve is non linear, estimating discharge across a transect in a braided river from the aggregated width will be different from the one obtained after the summation of discharges of the individual threads.

This study presents a robust methodology and is a step towards obtaining first order estimates of formative discharge in ungauged river basins solely from remote sensing images. It can be used for the sustainable river development and management to ensure regional water security, especially in the regions where river discharge is not readily available.

Appendix A: Dataset

A1 Satellite images

Detailed specification of satellite data (Landsat and Sentinel-1) used in this study. Table A1

Landsat-TM & Landsat-8				
River	**Date**	**Scene ID**	**Satellite**	**Gauge station**
Brahmaputra	2009-01-18	LT51380432009018KHC01	L-TM	25.18/89.66
Brahmaputra	2009-02-19	LT51380432009050KHC00	L-TM	25.18/89.66
Brahmaputra	2014-03-21	LC81380432014080LGN00	L-8	25.18/89.66
Brahmaputra	2014-04-22	LC81380432014112LGN00	L-8	25.18/89.66

Brahmaputra	2014-10-31	LC81380432014304LGN00	L-8	25.18/89.66
Brahmaputra	2013-11-29	LC81380432013333LGN00	L-8	25.18/89.66
Brahmaputra	2014-12-02	LC81380432014336LGN00	L-8	25.18/89.66
Chenab	2014-01-04	LC81500402014004LGN00	L-8	29.35/71.30
Chenab	2018-02-16	LC81500402018047LGN00	L-8	29.35/71.30
Chenab	2015-04-13	LC81500402015103LGN00	L-8	29.35/71.30
Chenab	2014-05-28	LC81500402014148LGN00	L-8	29.35/71.30
Chenab	2014-06-29	LC81500402014180LGN00	L-8	29.35/71.30
Chenab	2014-07-15	LC81500402014196LGN00	L-8	29.35/71.30
Chenab	2014-10-19	LC81500402014292LGN00	L-8	29.35/71.30
Chenab	2013-11-01	LC81500402013305LGN00	L-8	29.35/71.30
Chenab	2014-12-06	LC81500402014340LGN00	L-8	29.35/71.30
Ganga	2015-02-11	LC81390432015042LGN01	L-8	24.83/87.92
Ganga	2015-03-15	LC81390432015074LGN00	L-8	24.83/87.92
Ganga	2013-04-02	LT51390432010092KHC00	L-8	24.83/87.92
Ganga	2014-06-16	LC81390432014167LGN00	L-8	24.83/87.92
Ganga	2014-11-23	LC81390432014327LGN00	L-8	24.83/87.92
Ganga	2009-01-18	LT51380432009018KHC01	L-TM	24.08/89.03
Ganga	2009-02-19	LT51380432009050KHC00	L-TM	24.08/89.03
Ganga	2014-03-21	LC81380432014080LGN00	L-8	24.08/89.03
Ganga	2014-04-22	LC81380432014112LGN00	L-8	24.08/89.03
Ganga	2014-10-31	LC81380432014304LGN00	L-8	24.08/89.03
Ganga	2013-11-29	LC81380432013333LGN00	L-8	24.08/89.03
Ganga	2014-12-02	LC81380432014336LGN00	L-8	24.08/89.03
Indus	2015-01-05	LC81520422015005LGN00	L-8	25.35/68.35
Indus	2017-02-11	LC81520422017042LGN00	L-8	25.35/68.35
Indus	2015-03-10	LC81520422015069LGN00	L-8	25.35/68.35
Indus	2014-04-24	LC81520422014114LGN00	L-8	25.35/68.35
Indus	2014-06-27	LC81520422014178LGN00	L-8	25.35/68.35
Indus	2014-10-17	LC81520422014290LGN00	L-8	25.35/68.35
Indus	2014-11-18	LC81520422014162LGN00	L-8	25.35/68.35
Kosi	1991-01-15	LT51400421991015ISP00	L-TM	26.52/86.92
Kosi	2011-02-07	LT51400422011038BKT00	L-TM	26.52/86.92
Kosi	1992-03-06	LT51400421992066ISP00	L-TM	26.52/86.92
Kosi	2018-05-01	LC81400422018121LGN00	L-8	26.52/86.92

Kosi	2015-09-30	LC81400422015273LGN01	L-8	26.52/86.92
Kosi	2000-10-14	LE71400422000288SGS00	L-TM	26.52/86.92
Kosi	2013-11-11	LC81400422013315LGN00	L-TM	26.52/86.92
Kosi	2002-12-07	LE71400422002341SGS00	L-TM	26.52/86.92
Teesta	2014-04-22	LC81380422014112LGN00	L-8	26.33/88.87
Teesta	2014-10-31	LC81380422014304LGN00	L-8	26.33/88.87
Teesta	2014-11-16	LC81380422014320LGN00	L-8	26.33/88.87
Teesta	2014-12-02	LC81380422014336LGN00	L-8	26.33/88.87
Teesta	2015-03-08	LC81380422015067LGN00	L-8	25.70/89.50
Teesta	2014-04-22	LC81380422014112LGN00	L-8	25.70/89.50
Teesta	2014-10-31	LC81380422014304LGN00	L-8	25.70/89.50
Teesta	2014-12-02	LC81380422014336LGN00	L-8	25.70/89.50
Sentinel-1A				
Ganga	2017-10-17	S1A_IW_GRDH ⋯ _31A9_Cal_Spk_TC	S-1A	24.83/87.92
Ganga	2018-07-20	S1A_IW_GRDH ⋯ _BE68_Cal_Spk_TC	S-1A	24.83/87.92
Ganga	2018-05-18	S1A_IW_GRDH ⋯ _114F_Cal_Spk_TC	S-1A	24.83/87.92
Ganga	2018-08-10	S1A_IW_GRDH ⋯ _6C38_Cal_Spk_TC	S-1A	24.83/87.92
Ganga	2018-09-06	S1A_IW_GRDH ⋯ _4CBB_Cal_Spk_TC	S-1A	24.83/87.92
Ganga	2016-04-13	S1A_IW_GRDH ⋯ _4BF4_Cal_Spk_TC	S-1A	24.83/87.92
Ganga	2018-01-18	S1A_IW_GRDH ⋯ _831D_Cal_Spk_TC	S-1A	24.83/87.92
Ganga	2017-09-27	S1A_IW_GRDH ⋯ _2DC4_Cal_Spk_TC	S-1A	24.08/89.03
Ganga	2018-05-13	S1A_IW_GRDH ⋯ _EF71_Cal_Spk_TC	S-1A	24.08/89.03
Ganga	2018-06-08	S1A_IW_GRDH ⋯ _035D_Cal_Spk_TC	S-1A	24.08/89.03
Ganga	2018-07-12	S1A_IW_GRDH ⋯ _8CBA_Cal_Spk_TC	S-1A	24.08/89.03
Ganga	2018-08-17	S1A_IW_GRDH ⋯ _EF93_Cal_Spk_TC	S-1A	24.08/89.03
Brahamputra	2018-07-14	S1A_IW_GRDH ⋯ _2752_Cal_Spk_TC	S-1A	25.18/89.66
Brahamputra	2017-11-14	S1A_IW_GRDH ⋯ _BA85_TC_Cal	S-1A	25.18/89.66
Brahamputra	2018-05-15	S1A_IW_GRDH ⋯ _9533_Cal_Spk_TC	S-1A	25.18/89.66
Brahamputra	2017-09-17	S1A_IW_GRDH ⋯ _E022_Cal_Spk_TC	S-1A	25.18/89.66
Brahamputra	2018-06-18	S1A_IW_GRDH ⋯ _8D0F_Cal_Spk_TC	S-1A	25.18/89.66
Brahamputra	2018-08-19	S1A_IW_GRDH ⋯ _173D_Cal_Spk_TC	S-1A	25.18/89.66
Chenab	2018-09-07	S1A_IW_GRDH ⋯ _3240_Cal_Spk_TC	S-1A	29.35/71.30
Chenab	2018-08-14	S1A_IW_GRDH ⋯ _A3CB_Cal_Spk_TC	S-1A	29.35/71.30
Chenab	2018-03-19	S1A_IW_GRDH ⋯ _2E5E_Spk_TC	S-1A	29.35/71.30
Chenab	2018-02-23	S1A_IW_GRDH ⋯ _741E_TC_Cal_Spk	S-1A	29.35/71.30

Indus	2018-07-10	S1A_IW_GRDH ⋯ _4B89_Cal_Spk_TC	S-1A	25.35/68.35
Indus	2018-05-11	S1A_IW_GRDH ⋯ _CE83_Cal_Spk_TC	S-1A	25.35/68.35
Indus	2017-09-13	S1A_IW_GRDH ⋯ _7DD5_Cal_Spk_TC	S-1A	25.35/68.35
Indus	2018-08-27	S1A_IW_GRDH ⋯ _DA34_Cal_Spk_TC	S-1A	25.35/68.35
Teesta	2017-09-03	S1A_IW_GRDH ⋯ _32D8_Cal_Spk_T	S-1A	25.70/89.50
Teesta	2018-01-13	S1A_IW_GRDH ⋯ _022569	S-1A	25.70/89.50
Teesta	2018-05-13	S1A_IW_GRDH ⋯ _021886	S-1A	25.70/89.50
Teesta	2018-06-06	S1A_IW_GRDH ⋯ _022236	S-1A	25.70/89.50
Teesta	2018-07-12	S1A_IW_GRDH ⋯ _022761	S-1A	25.70/89.50
Teesta	2018-08-29	S1A_IW_GRDH ⋯ _023461	S-1A	25.70/89.50
Teesta	2017-09-03	S1A_IW_GRDH ⋯ _32D8_Cal_Spk_TC	S-1A	26.33/88.87
Teesta	2018-01-13	S1A_IW_GRDH ⋯ _50B1_Cal_Spk_TC	S-1A	26.33/88.87
Teesta	2018-05-13	S1A_IW_GRDH ⋯ _D8D7_Cal_Spk_TC	S-1A	26.33/88.87
Teesta	2018-06-06	S1A_IW_GRDH ⋯ _1753_Cal_Cal_TC	S-1A	26.33/88.87
Teesta	2018-07-12	S1A_IW_GRDH ⋯ _F499_Cal_Spk_TC	S-1A	26.33/88.87
Teesta	2018-08-29	S1A_IW_GRDH ⋯ _341E_Cal_Spk_TC	S-1A	26.33/88.87
Kosi	2018-08-18	S1A_IW_GRDH ⋯ _8CB2_Cal_Spk_TC	S-1A	26.52/86.92
Kosi	2018-06-19	S1A_IW_GRDH ⋯ _9B41_Cal_Spk_TC	S-1A	26.52/86.92
Kosi	2017-04-25	S1A_IW_GRDH ⋯ _32C5_Cal_Spk_TC	S-1A	26.52/86.92
Kosi	2017-07-30	S1A_IW_GRDH ⋯ _2658_Cal_Spk_TC	S-1A	26.52/86.92

Table A1 Details of the Landsat-8 (L-8), Landsat-TM (L-TM) and Sentinel-1A (S-1A) satellite images used in this study. Gauge station is the location (lat/lon) of nearest in-situ discharge measurement stations.

A2 Description of satellite and in-situ dataset

Table A2 contains a detailed description of in-situ discharge data for different rivers used in this study. This includes, data source, location of gauge station and period of measurement.

A3 Glossary

Appendix B: Satellite image processing

B0.1 Identification of river channels

To identify the river and non river pixels, we have used the infra-red bands of Landsat-TM and Landsat-8 images. In Landsat-TM, the infra-red $(0.76 - 0.90\,\mu\mathrm{m})$ wavelength corresponds to band 4 whereas, in Landsat-8 image, it corresponds to band 5 $(0.85 - 0.88\,\mu\mathrm{m})$.

In-situ data (discharge)						Satellite images (years)
River	Station	Location		Period	Source	
		Longitude (degree)	Latitude (degree)			
Teesta	Anderson	88.87	26.33	1965-1971	RivDIS	2014, 2015, 2017, 2018
	Kaunia	89.50	25.70	1969-1975	RivDIS	2014, 2017, 2018
Kosi	Bhimnagar	86.92	26.52	2002-2014	Kosi barrage Birpur	1991, 1992, 2000, 2002 2011, 2013, 2015, 2017, 2018
Chenab	Panjnad	71.30	29.35	1973-1979	RivDIS	2013, 2014, 2015, 2018
Indus	Kotri	68.35	25.35	1973-1979	RivDIS	2014, 2015, 2017, 2018
Ganga	Farakka	87.92	24.83	1949-1973 1978-2007	RivDIS & CWC	2013, 2014, 2015, 2016, 2018
	Paksay	89.03	24.08	1965-1975 1996-2005	RivDIS & Dhaka Univ.	2009, 2013, 2014, 2017, 2018
Brahmaputra	Bahadurabad	89.66	25.18	1969-1975 1996-2005	RivDIS & Dhaka Univ.	2009, 2013, 2014, 2017, 2018

Table A2. Satellite images used for the extraction of channels width. In-situ discharge data is freely available and were downloaded from (http://www.rivdis.sr.unh.edu/maps/asi/).

We obtained an optimal threshold value by using the algorithm initially proposed by Yanni and Horne (1994). We than used the optimal threshold value to separate water and dry pixels from Landsat satellite images. The algorithm initiate by selecting a threshold as a midpoint value that lies in between the maximum and minimum gray level intensity (gi) as $\mathrm{gi}_{\mathrm{mid}} = (\mathrm{gi}_{\mathrm{max}} + \mathrm{gi}_{\mathrm{min}})/2$, where $\mathrm{gi}_{\mathrm{max}}$ is the highest and $\mathrm{gi}_{\mathrm{min}}$ is the lowest gray level intensity. Based on this initial threshold, the image pixels are clustered into foreground and background objects. After each iteration the threshold value is updated using the mean intensity of both the clusters. Finally the algorithm terminates when the threshold converges.

B0.2 Removal of artefacts

Thresholding a gray scale input satellite image into binary class (water and dry pixels) produces spurious features. These consist of wet pixels that get classified as dry or of isolated water pixels that appear randomly in the binary images. Clusters (usually 2-3 pixels in size) that appear inside the river network do not corresponds to bars or islands. They appear to be more frequent in the areas where strong reflection from the bed sediment cause water pixels to appear more like a sand. Isolated water pixels that do not belong to the river are disconnected and located in water-logged areas. We have identified both of

Type	Defination	Remarks	Source
Instantaneous discharge	discharge at any given time in space	usually measured at gauge stations installed on rivers	Chow (2010), Navratil et al. (2006)
Monthly average discharge	average discharge in a given month of the year	calculated by taking the mean of each month for the entire period of record	Chow (2010)
Annual average discharge	average discharge in a given year or time series	calculated by taking the mean of total discharge in a year or period	Chow (2010)
Median discharge	median value of discharge in a given year or period	calculated by finding the median value from the discharge time series of a given period	Blench (1957)
Bankfull discharge	discharge that completely fills the channel.	occurs once every year or in every two years	Wolman and Miller (1960), Navratil et al. (2006) (Rhoads, 2020, p. 145)
Formative discharge	derived discharge that would result in the same hydraulic geometry as the long-term hydrograph.	corresponds to average annual discharge, median flood discharge, and bankfull discharge	Leopold and Maddock (1953), Wolman and Miller (1960), Bolla Pittaluga et al. (2014) (Rhoads, 2020, p. 144)

Table A3. A summary of terminology used for different discharges in this study.

these type errors from binary image and reprocess to remove them automatically. While doing this we first define a seed point inside the main channel and run the flood filling algorithm (Mehnert and Jackway, 1997; Bernander et al., 2013; Fan et al., 2005). This identify water pixels in a river channel those are connected and remove the isolated water pixels those have poor connectivity (Fig. B1).

B0.3 Extraction of channel's skeleton and contour

Our channel width extraction algorithm requires to river's centerline and boundary. A river centerline often called skeleton in computer vision corresponds to its median axis. To identify the river skeleton, we have used a thinning algorithm to extract river's centerline. The algorithm iteratively reduces the boundary pixels in a way that preserves its topology (for example eroding pixels must not alter the geometric properties of the object studied) and connectivity (Fig. B2 a). The final skeleton is centered within the object and reflects its geometrical properties (Zhang and Suen, 1984; Baruch, 1988; Lam et al., 1992; Chatbri et al., 2015). The thinning algorithms produces several small centre line segments, often less than 300 meter in length, that are disconnected from the channel network at one end. These segments of the skeleton are too small to be considered as part of the river network. For our purpose we consider such segments as noise and filter them out. We do this iteratively, by looking for skeleton segments those are disconnected from the skeleton network at one end. To extract the channel banks, we

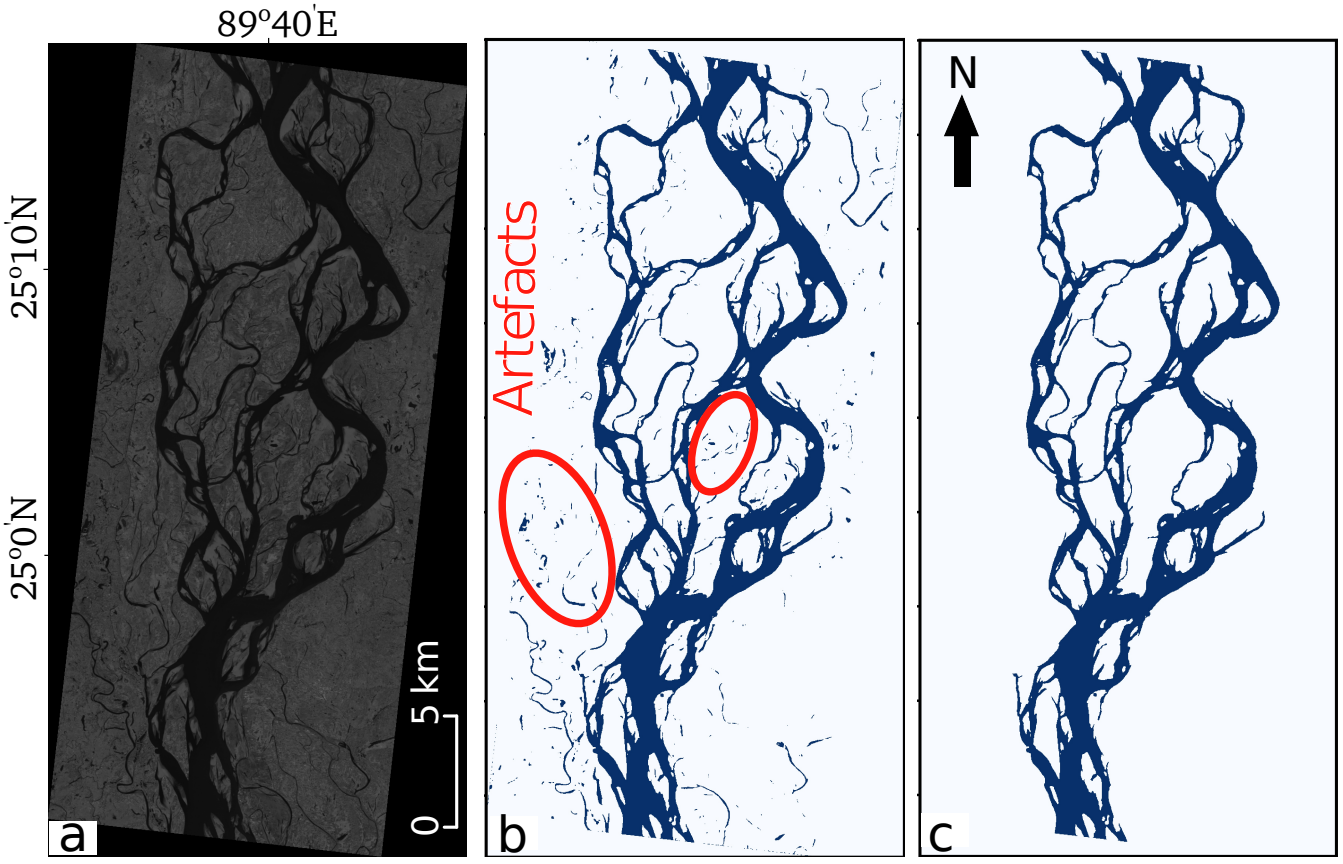

Figure B1. (a) Input Landsat-8 image of short wave infra-red wavelength is threshold to create binary image having water (blue) and dry (white) pixels. (b) Binary image with isolated water patches and artefacts and (c) removed artefacts (image source: Landsat-TM, 29 November 2013).

have applied a contour extraction algorithm that detects the outer boundary of a channel (Fig. B2). The algorithm relies on a pixel-neighbourhood analysis, where a pixel in a binary image is considered a contour pixel, if it has at least one background neighbour (Chatbri et al., 2015).

B0.4 Channel's width calculation

Once the satellite images are processed to extract skeleton and channel's banks, we then proceed to extract the width of each channels. We do this by measuring the distance from the centre of a channel to its banks orthogonally to the flow. From the skeleton of the image we draw a perpendicular line to the river bank and measure the the euclidean distance (Fig. B3). In case of a braided river, especially near the junctions where more than two river join or bifurcate form a complex network. At such locations our algorithm fails to measure correct width. To circumvent this we identify all the junctions from river skeleton

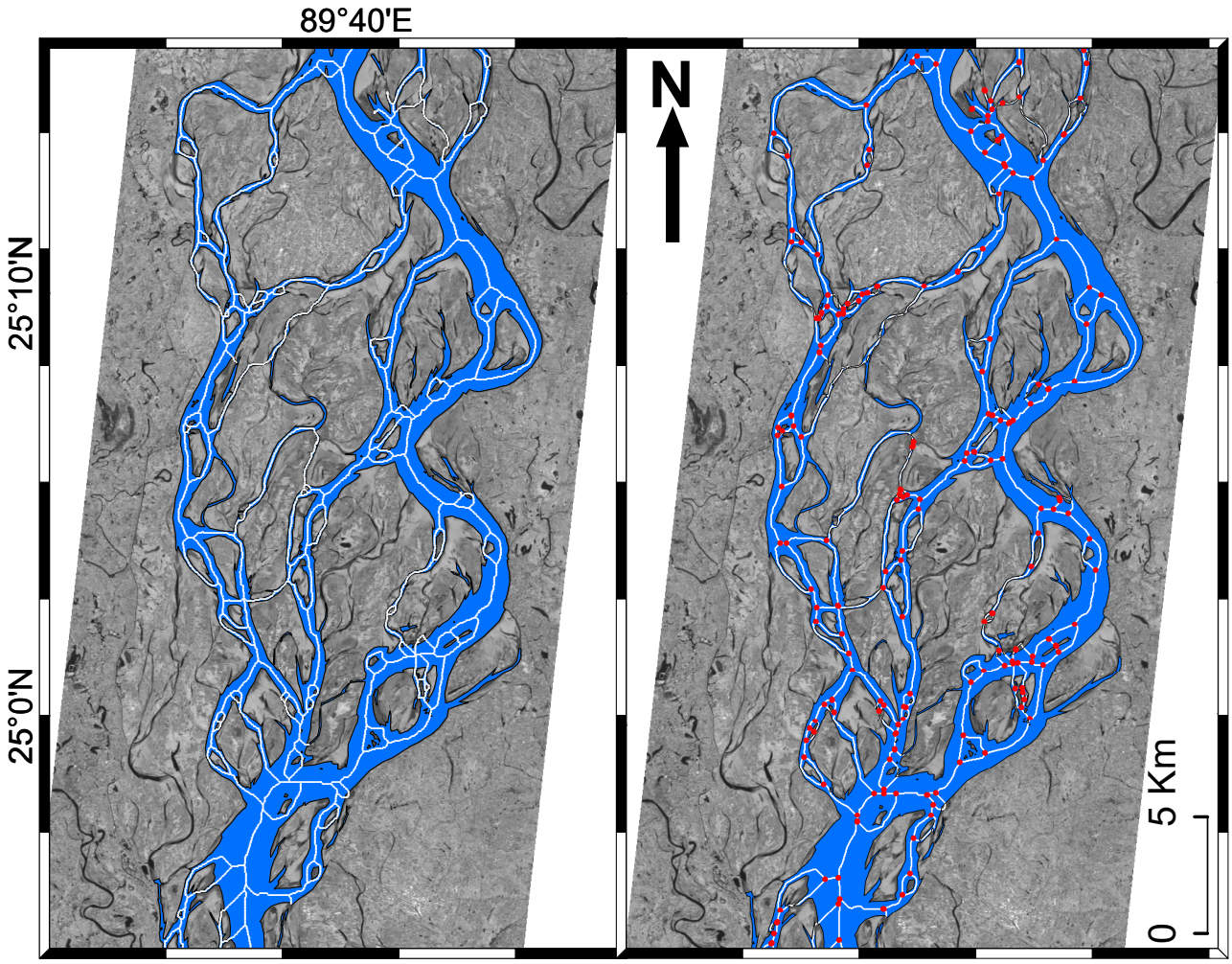

Figure B2. In left: river center line (skeleton) and boundary (contour) are superimposed on Landsat-8 satellite image. In right: image illustrates the stream junction identified on skeleton (image source: Landsat-TM, 29 November 2013).

(Fig. B2b). In the proximity of junction we consider an area of 5 pixels and define them as a zone of channel's confluence and diffluence. In this zone we avoid to calculate the width of the channels.

Finally, we draw perpendicular transects from each pixel of the skeleton to both side of the channel and calculate the distance from any point (x, y) on the skeleton to its corresponding left (x_1, y_1) and right (x_2, y_2) points on the channel boundary (Fig. B3). We then sum these widths to get the total width across a transect. For simplicity, at every one kilometer distance along the channel we compute the most probable width of each channels across a river section. Finally, the discharges through a section can be calculated along an entire reach (Fig. B3).

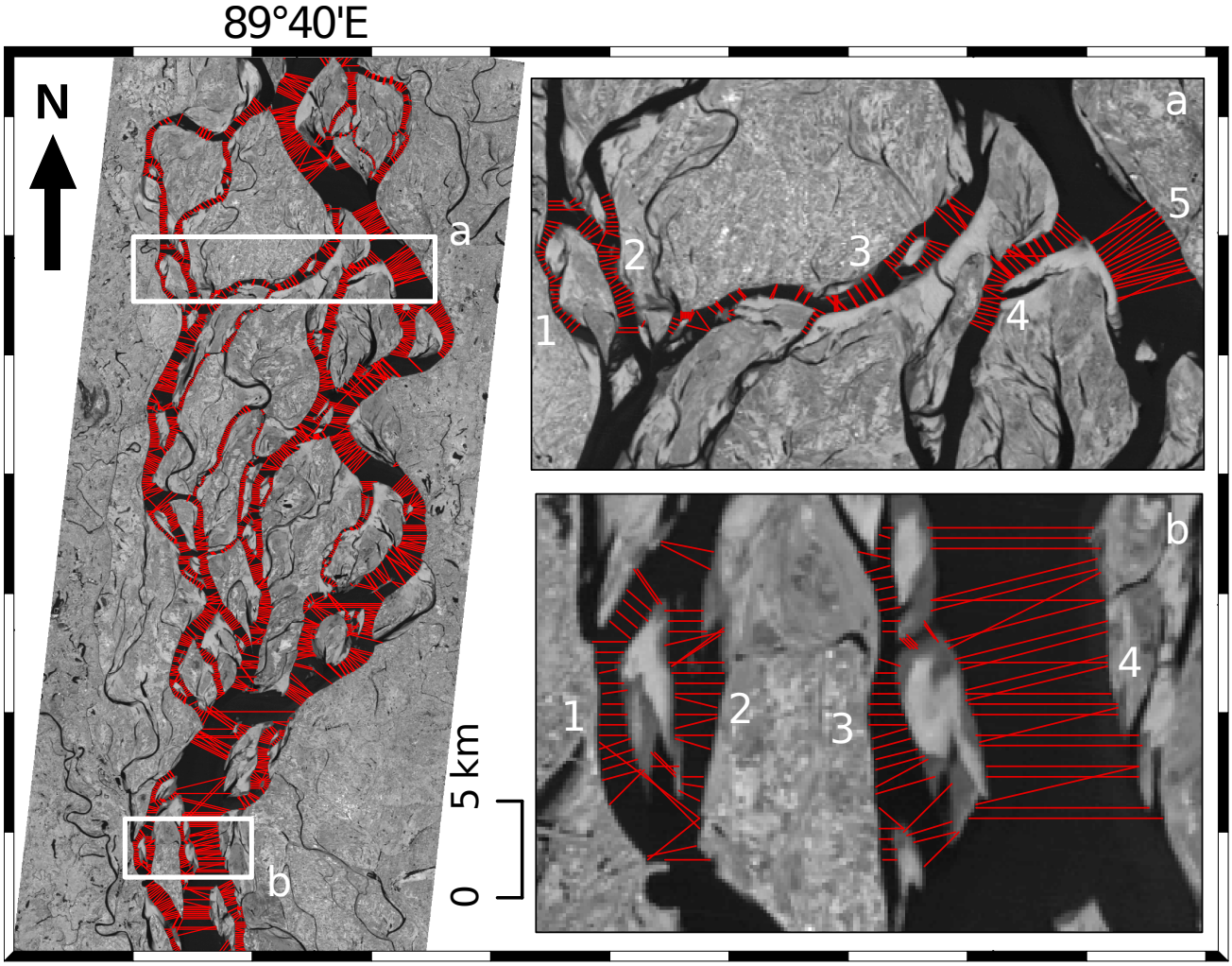

Figure B3. Width extracted across each of the individual channels. Image in the right illustrates the reach lengths (in boxes) over which most probable width of each channels is calculated (image source: Landsat-TM, 29 November 2013).

Appendix C: Measured Vs. Estimated discharge

C1 Hydrograph of the Kosi River

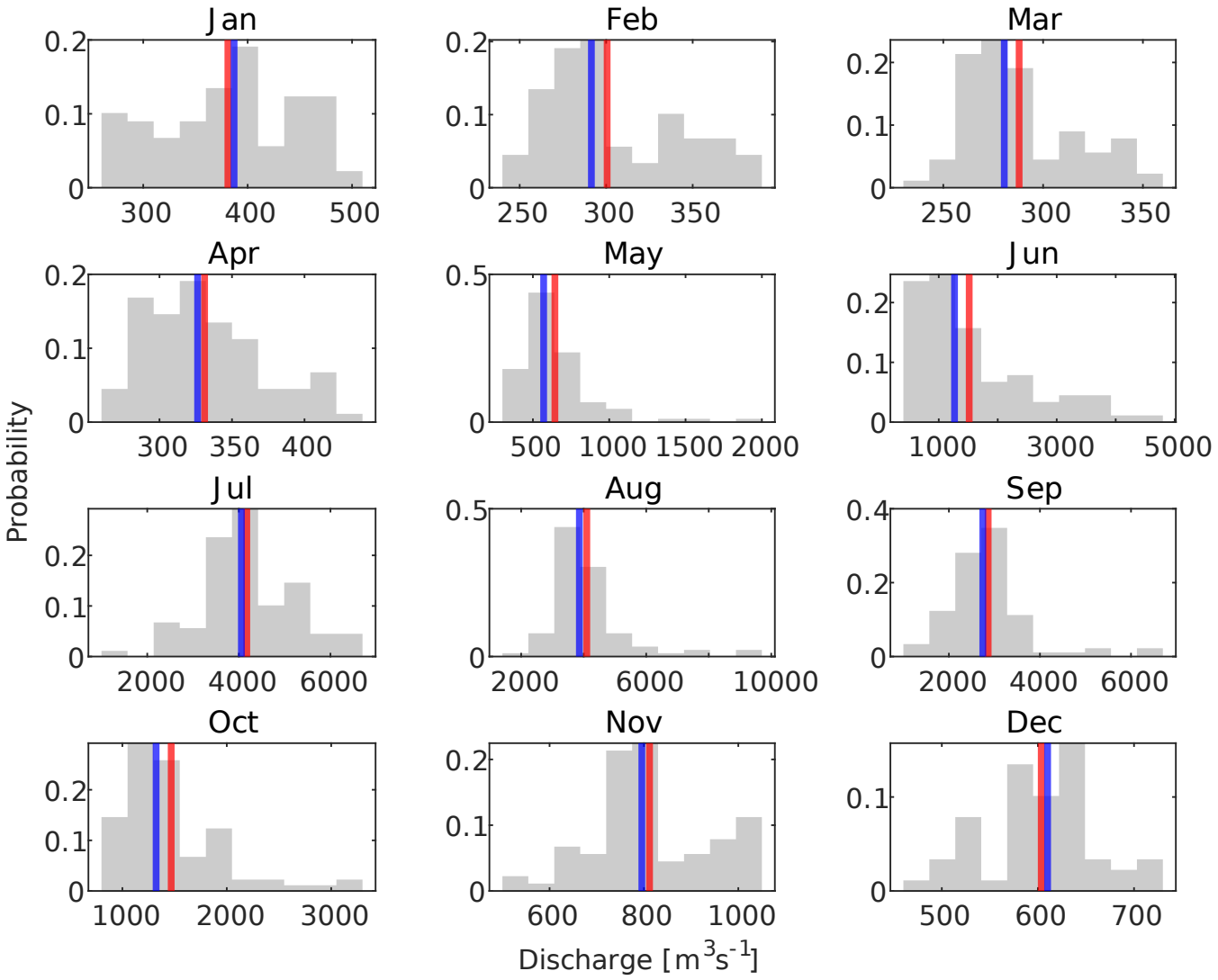

Figure C1. Histogram of daily discharge of the Kosi River measured at the Bhimnagar barrage in 2011, 2013, and 2014. Vertical lines in red and blue are the mean and median values of the probability distribution.

C2 Evolution of discharge time series

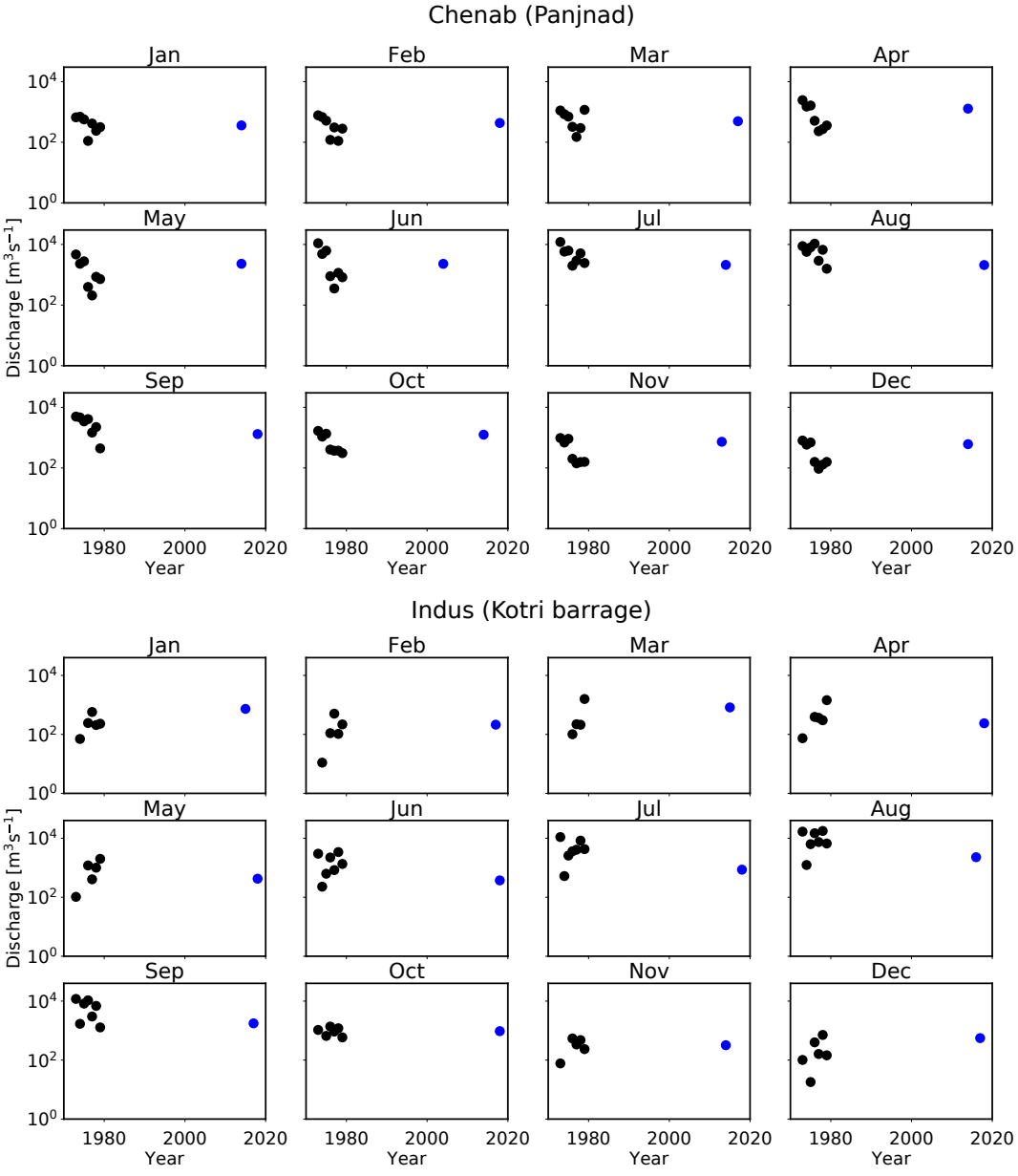

Figure C2. Time series of discharge of the Chenab and Indus river (circles in black) measured at the ground station (Panjnad and Kotri barrage). Circle in blue is the discharge estimated from satellite images

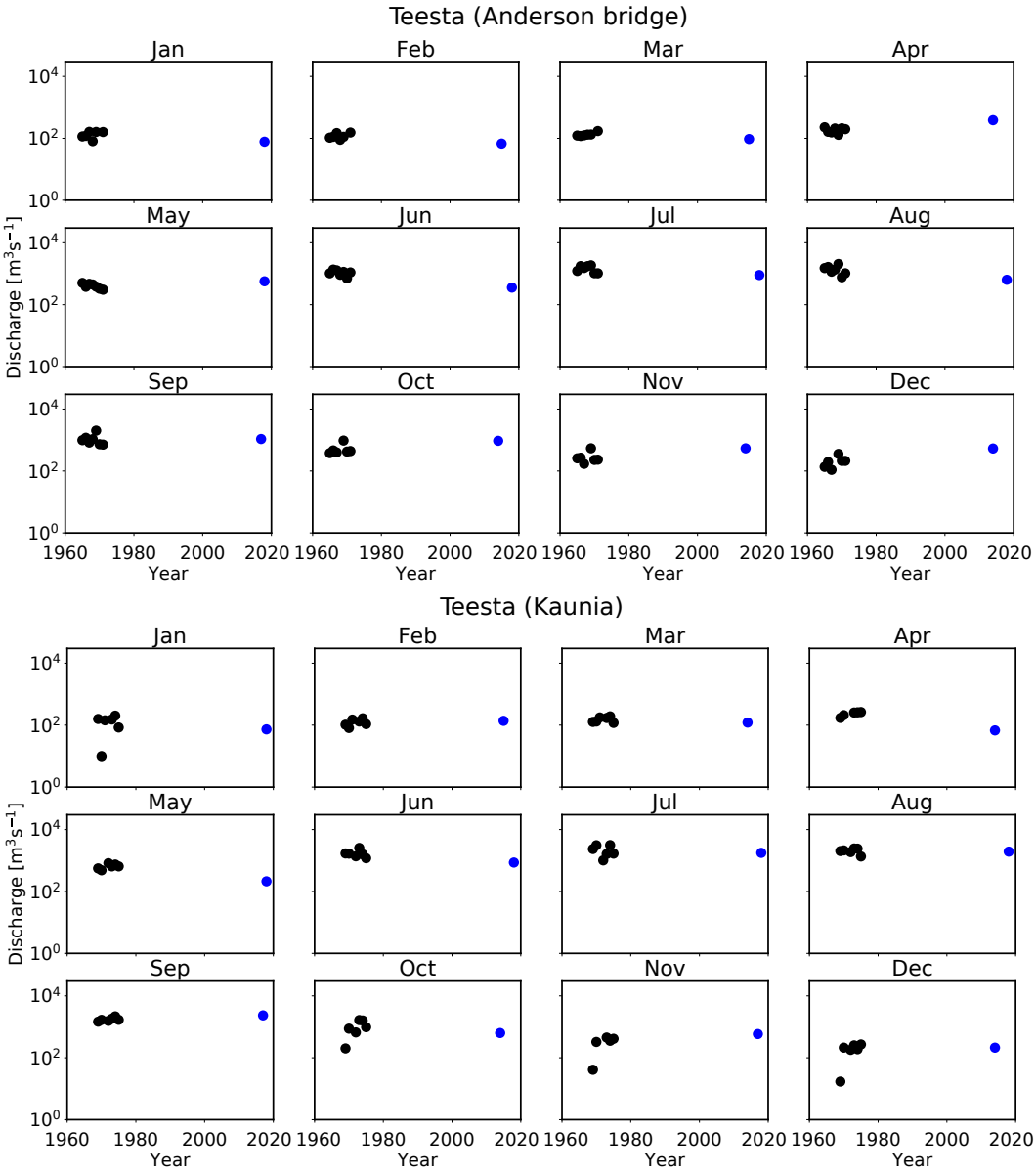

Figure C3. Time series of discharge of the Teesta River (circles in black) measured at the ground station (Anderson bridge and Kaunia). Circle in blue is the discharge estimated from satellite images.

C3 Comparison of mean annual discharge with GRWL database

Allen and Pavelsky (2018) measured the width of the global rivers from Landsat images for the month when they commonly flow near mean discharge. In their database, Global River Width from Landsat (GRWL), for braided river they have reported the aggregated width of all the active threads. This width can not be used to estimate discharge from our regime curve that we established for the Himalayan Rivers. Our regime curve relates to the measurement of hydraulic geometry of individual threads of braided and meandering rivers (Gaurav et al., 2014, 2017), therefore it is applicable only at the thread scale. Since the resulting regime curve is non linear, estimating discharge across a transect in a braided river from the aggregated width will be different from the discharge obtained from the summation of discharge of the individual threads.

To overcome this, we have used binary water mask images from GRWL database to extract width of the individual threads. We then use these threads to estimate their discharge using our regime curve (equations. 4 and 6 in the manuscript). We observed for most of our rivers, discharge estimated from threads width extracted from the GRWL database falls within the same order of magnitude to the yearly average discharge measured at the corresponding gauge stations (Table C1).

River	Station	$\langle Q_{insitu} \rangle$ $m^3 s^{-1}$	$\langle Q_{sat.} \rangle$ $m^3 s^{-1}$	$\langle Q_{GRWL} \rangle$ $m^3 s^{-1}$
Teesta	Anderson	605 ± 109	638 ± 165	408 ± 177
Teesta	Kaunia	924 ± 144	745 ± 155	400 ± 110
Kosi	Bhimnagar	1559 ± 313	1810 ± 380	2936 ± 625
Chenab	Panjnad	2500 ± 961	1275 ± 268	937 ± 344
Indus	Kotri	3745 ± 825	794 ± 162	218 ± 102
Ganga	Farakka	11477 ± 2279	10593 ± 2225	15959 ± 9616
Ganga	Paksay	12080 ± 2403	11605 ± 2438	5679 ± 3310
Brahmaputra	Bahadurabad	21751 ± 2942	21717 ± 4740	11149 ± 5122

Table C1. Annual average discharge measured at the gauge station and estimated from satellite images. $\langle Q_{GRWL} \rangle$ is the discharge estimated from binary water mask from GRWL database from Allen and Pavelsky (2018).

Author contributions. KG, AVS and FM have conceptualised the study, KG collected the field data, AVS and KG developed the algorithm to process satellite images, AK has processed the Sentinel-1 satellite images. KG has written the manuscript and FM, RS and SKT have reviewed. All authors discussed the results and contributed to the final manuscript.

Competing interests. The authors declare that they have no conflict of interest

Acknowledgements. K.G and AV.S acknowledge the Ministry of Earth Sciences, Government of India for research funding through Letter no.: MoES/PAMC/H & M/84/2016-PC-II. K.G would like thank Dr. Olivier Devauchelle for fruitful discussion. We thank Mr. Hasnat Jaman, a former student of the Geology department of University of Dhaka for providing the discharge data for the Ganga and Brahmaputra rivers. Satellite imagery courtesy of USGS/NASA and ESA. We are thankful to Central Water commission, Ministry of water resources, New Delhi, Engineers of the Investigation and research division of the Kosi river Project and global river discharge databases (RivDIS v1.0) for providing the in-situ measurement of discharge

References

Allen, G. H. and Pavelsky, T. M.: Global extent of rivers and streams, Science, 361, 585–588, 2018.

Alsdorf, D. E., Melack, J. M., Dunne, T., Mertes, L. A., Hess, L. L., and Smith, L. C.: Interferometric radar measurements of water level changes on the Amazon flood plain, Nature, 404, 174–177, 2000.

Alsdorf, D. E., Rodríguez, E., and Lettenmaier, D. P.: Measuring surface water from space, Reviews of Geophysics, 45, 2007.

Amitrano, D., Di Martino, G., Iodice, A., Riccio, D., and Ruello, G.: Unsupervised Rapid Flood Mapping Using Sentinel-1 GRD SAR Images, IEEE Transactions on Geoscience and Remote Sensing, 56, 3290–3299, 2018.

Andermann, C., Longuevergne, L., Bonnet, S., Crave, A., Davy, P., and Gloaguen, R.: Impact of transient groundwater storage on the discharge of Himalayan rivers, Nature Geoscience, 5, ngeo1356, 2012.

Andreadis, K. M., Clark, E. A., Lettenmaier, D. P., and Alsdorf, D. E.: Prospects for river discharge and depth estimation through assimilation of swath-altimetry into a raster-based hydrodynamics model, Geophysical Research Letters, 34, 2007.

Ashmore, P. and Sauks, E.: Prediction of discharge from water surface width in a braided river with implications for at-a-station hydraulic geometry, Water Resources Research, 42, 2006.

Baruch, O.: Line thinning by line following, Pattern Recognition Letters, 8, 271–276, 1988.

Bernander, K. B., Gustavsson, K., Selig, B., Sintorn, I.-M., and Hendriks, C. L. L.: Improving the stochastic watershed, Pattern Recognition Letters, 34, 993–1000, 2013.

Bjerklie, D. M., Moller, D., Smith, L. C., and Dingman, S. L.: Estimating discharge in rivers using remotely sensed hydraulic information, Journal of Hydrology, 309, 191–209, 2005.

Blench, T.: Regime behaviour of canals and rivers, Butterworths Scientific Publications London, 1957.

Blom, A., Arkesteijn, L., Chavarrías, V., and Viparelli, E.: The equilibrium alluvial river under variable flow and its channel-forming discharge, Journal of Geophysical Research: Earth Surface, 122, 1924–1948, 2017.

Bolla Pittaluga, M., Luchi, R., and Seminara, G.: On the equilibrium profile of river beds, Journal of Geophysical Research: Earth Surface, 119, 317–332, 2014.

Bookhagen, B. and Burbank, D. W.: Toward a complete Himalayan hydrological budget: Spatiotemporal distribution of snowmelt and rainfall and their impact on river discharge, Journal of Geophysical Research: Earth Surface, 115, 2010.

Chatbri, H., Kameyama, K., and Kwan, P.: A comparative study using contours and skeletons as shape representations for binary image matching, Pattern Recognition Letters, 2015.

Chow, V.: Applied hydrology, Tata McGraw-Hill Education, 2010.

Delorme, P., Voller, V., Paola, C., Devauchelle, O., Lajeunesse, É., Barrier, L., and Métivier, F.: Self-similar growth of a bimodal laboratory fan, Earth Surface Dynamics, 5, 239–252, 2017.

Dunne, K. B. and Jerolmack, D. J.: What sets river width?, Science Advances, 6, eabc1505, 2020.

Durand, M., Gleason, C., Garambois, P.-A., Bjerklie, D., Smith, L., Roux, H., Rodriguez, E., Bates, P. D., Pavelsky, T. M., Monnier, J., et al.: An intercomparison of remote sensing river discharge estimation algorithms from measurements of river height, width, and slope, Water Resources Research, 52, 4527–4549, 2016.

Fan, J., Zeng, G., Body, M., and Hacid, M.-S.: Seeded region growing: an extensive and comparative study, Pattern recognition letters, 26, 1139–1156, 2005.

Frazier, P. S., Page, K. J., et al.: Water body detection and delineation with Landsat TM data, Photogrammetric Engineering and Remote Sensing, 66, 1461–1468, 2000.

Gaurav, K., Métivier, F., Devauchelle, O., Sinha, R., Chauvet, H., Houssais, M., and Bouquerel, H.: Morphology of the Kosi megafan channels, Earth Surface Dynamics Discussions, 2, 1023–1046, 2014.

Gaurav, K., Tandon, S., Devauchelle, O., Sinha, R., and Métivier, F.: A single width–discharge regime relationship for individual threads of braided and meandering rivers from the Himalayan Foreland, Geomorphology, 295, 126–133, 2017.

Gleason, C. J. and Smith, L. C.: Toward global mapping of river discharge using satellite images and at-many-stations hydraulic geometry, Proceedings of the National Academy of Sciences, 111, 4788–4791, 2014.

Gleason, C. J., Wada, Y., and Wang, J.: A hybrid of optical remote sensing and hydrological modeling improves water balance estimation, Journal of Advances in Modeling Earth Systems, 10, 2–17, 2018.

Glover, R. and Florey, Q.: Stable channel profiles, Hydraulic laboratory report HYD no. 325, US Department of the Interior, Bureau of Reclamation, Design and Construction Division, 1951., 1951.

Henderson, F. M.: Stability of alluvial channels, Transactions of the American Society of Civil Engineers, 128, 657–686, 1963.

Inam, A., Clift, P. D., Giosan, L., Tabrez, A. R., Tahir, M., Rabbani, M. M., and Danish, M.: The geographic, geological and oceanographic setting of the Indus River, Large rivers: geomorphology and management, pp. 333–345, 2007.

Inglis, C. C. and Lacey, G.: Meanders and their bearing on river training. Maritime and waterways engineering division., ICE Engineering Division Papers, 5, 3–24, 1947.

Julien, P.: Erosion and sedimentation, Cambridge university press, 1995.

Kebede, M. G., Wang, L., Li, X., and Hu, Z.: Remote sensing-based river discharge estimation for a small river flowing over the high mountain regions of the Tibetan Plateau, International Journal of Remote Sensing, 41, 3322–3345, 2020.

Khan, A. A., Pant, N. C., Sarkar, A., Tandon, S., Thamban, M., and Mahalinganathan, K.: The Himalayan cryosphere: a critical assessment and evaluation of glacial melt fraction in the Bhagirathi basin, Geoscience Frontiers, 8, 107–115, 2017.

Lacey, G.: Stable channels in alluvium (Includes Appendices)., in: Minutes of the Proceedings, vol. 229, pp. 259–292, Thomas Telford, Proceedings of the Institution of Civil Engineers, Landoon, 1930.

Lam, L., Lee, S.-W., and Suen, C. Y.: Thinning methodologies-a comprehensive survey, IEEE Transactions on pattern analysis and machine intelligence, 14, 869–885, 1992.

Leopold, L. B. and Maddock, T.: The hydraulic geometry of stream channels and some physiographic implications, vol. 252, US Government Printing Office, 1953.

Marcus, W. A. and Fonstad, M. A.: Optical remote mapping of rivers at sub-meter resolutions and watershed extents, Earth Surface Processes and Landforms, 33, 4–24, 2008.

Martinis, S., Plank, S., and Ćwik, K.: The Use of Sentinel-1 Time-Series Data to Improve Flood Monitoring in Arid Areas, Remote Sensing, 10, 583, 2018.

Mehnert, A. and Jackway, P.: An improved seeded region growing algorithm, Pattern Recognition Letters, 18, 1065–1071, 1997.

Métivier, F., Devauchelle, O., Chauvet, H., Lajeunesse, E., Meunier, P., Ashmore, P., Blanckaert, K., Zhang, Z., Fan, Y., Liu, Y., et al.: Geometry of meandering and braided gravel-bed threads from the Bayanbulak Grassland, Tianshan, PR China, Earth Surface Dynamics, 4, 273–283, 2016.

Métivier, F., Lajeunesse, E., and Devauchelle, O.: Laboratory rivers: Lacey's law, threshold theory, and channel stability, Earth Surface Dynamics, 5, 187, 2017.

Moramarco, T., Barbetta, S., Bjerklie, D. M., Fulton, J. W., and Tarpanelli, A.: River Bathymetry Estimate and Discharge Assessment from Remote Sensing, Water Resources Research, 55, 6692–6711, 2019.

Navratil, O., Albert, M.-B., Herouin, E., and Gresillon, J.-M.: Determination of bankfull discharge magnitude and frequency: comparison of methods on 16 gravel-bed river reaches, Earth Surface Processes and Landforms: The Journal of the British Geomorphological Research Group, 31, 1345–1363, 2006.

Nykanen, D. K., Foufoula-Georgiou, E., and Sapozhnikov, V. B.: Study of spatial scaling in braided river patterns using synthetic aperture radar imagery, Water resources research, 34, 1795–1807, 1998.

Papa, F., Durand, F., Rossow, W. B., Rahman, A., and Bala, S. K.: Satellite altimeter-derived monthly discharge of the Ganga-Brahmaputra River and its seasonal to interannual variations from 1993 to 2008, Journal of Geophysical Research: Oceans (1978–2012), 115, 2010.

Papa, F., Bala, S. K., Pandey, R. K., Durand, F., Gopalakrishna, V., Rahman, A., and Rossow, W. B.: Ganga-Brahmaputra river discharge from Jason-2 radar altimetry: An update to the long-term satellite-derived estimates of continental freshwater forcing flux into the Bay of Bengal, Journal of Geophysical Research: Oceans (1978–2012), 117, 2012.

Passalacqua, P., Lanzoni, S., Paola, C., and Rinaldo, A.: Geomorphic signatures of deltaic processes and vegetation: The Ganges-Brahmaputra-Jamuna case study, Journal of Geophysical Research: Earth Surface, 118, 1838–1849, 2013.

Phillips, C. B. and Jerolmack, D. J.: Self-organization of river channels as a critical filter on climate signals, Science, 352, 694–697, 2016.

Rhoads, B. L.: River Dynamics: Geomorphology to Support Management, Cambridge University Press, 2020.

Ridler, T. and Calvard, S.: Picture thresholding using an iterative selection method, IEEE transactions on Systems, Man and Cybernetics, 8, 630–632, 1978.

Roy, N. and Sinha, R.: Effective discharge for suspended sediment transport of the Ganga River and its geomorphic implication, Geomorphology, 227, 18–30, 2014.

Schlaffer, S., Matgen, P., Hollaus, M., and Wagner, W.: Flood detection from multi-temporal SAR data using harmonic analysis and change detection, International Journal of Applied Earth Observation and Geoinformation, 38, 15–24, 2015.

Schumm, S. A. and Lichty, R. W.: Time, space, and causality in geomorphology, American journal of science, 263, 110–119, 1965.

Seizilles, G.: Forme d'équilibre d'une rivière, Ph.D. thesis, Paris 7, 2013.

Seizilles, G., Devauchelle, O., Lajeunesse, E., and Métivier, F.: Width of laminar laboratory rivers, Physical Review E, 87, 052 204, 2013.

Selim Yalin, M.: River mechanics, Pergamon, 1992.

Sezgin, M. et al.: Survey over image thresholding techniques and quantitative performance evaluation, Journal of Electronic imaging, 13, 146–168, 2004.

Singh, P. and Jain, S.: Snow and glacier melt in the Satluj River at Bhakra Dam in the western Himalayan region, Hydrological sciences journal, 47, 93–106, 2002.

Smith, L., Isacks, B., Forster, R., Bloom, A., and Preuss, I.: Estimation of discharge from braided glacial rivers using ERS 1 synthetic aperture radar: First results, Water Resources Research, 31, 1325–1329, 1995.

Smith, L. C.: Satellite remote sensing of river inundation area, stage, and discharge: A review, Hydrological processes, 11, 1427–1439, 1997.

Smith, L. C. and Pavelsky, T. M.: Estimation of river discharge, propagation speed, and hydraulic geometry from space: Lena River, Siberia, Water Resources Research, 44, 2008.

Smith, L. C., Isacks, B. L., Bloom, A. L., and Murray, A. B.: Estimation of discharge from three braided rivers using synthetic aperture radar satellite imagery: Potential application to ungaged basins, Water Resources Research, 32, 2021–2034, 1996.

Sun, W., Ishidaira, H., and Bastola, S.: Towards improving river discharge estimation in ungauged basins: calibration of rainfall-runoff models based on satellite observations of river flow width at basin outlet, Hydrology and Earth System Sciences, 14, 2011, 2010.

Thayyen, R. and Gergan, J.: Role of glaciers in watershed hydrology: a preliminary study of a" Himalayan catchment", The Cryosphere, 4, 115–128, 2010.

Twele, A., Cao, W., Plank, S., and Martinis, S.: Sentinel-1-based flood mapping: a fully automated processing chain, International Journal of Remote Sensing, 37, 2990–3004, 2016.

Wolman, M. G. and Leopold, L. B.: River flood plains: some observations on their formation, 1957.

Wolman, M. G. and Miller, J. P.: Magnitude and frequency of forces in geomorphic processes, The Journal of Geology, 68, 54–74, 1960.

Yanni, M. and Horne, E.: A new approach to dynamic thresholding, in: EUSIPCO'94: 9th European Conf. Sig. Process, vol. 1, pp. 34–44, 1994.

Zhang, T. and Suen, C. Y.: A fast parallel algorithm for thinning digital patterns, Communications of the ACM, 27, 236–239, 1984.